Stockholm University

Pressure-Induced Amorphization and Distinct Amorphous States of Clathrate Hydrates

Paulo H. B. Brant Carvalho

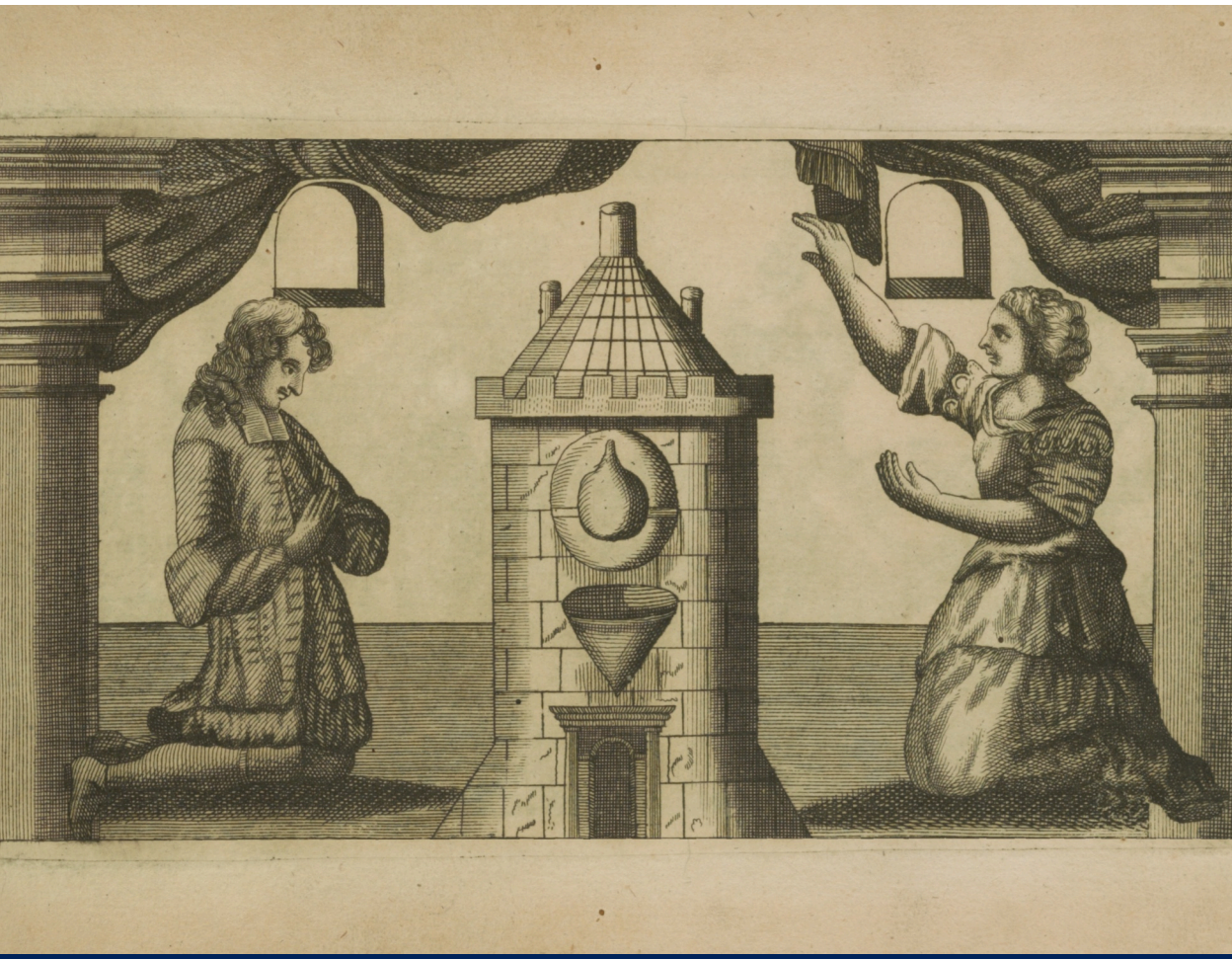

Doctoral Thesis in Physical Chemistry at Stockholm University, Sweden 2023

Pressure-Induced Amorphization and Distinct Amorphous States of Clathrate Hydrates

Paulo H. B. Brant Carvalho

Academic dissertation for the Degree of Doctor of Philosophy in Physical Chemistry at Stockholm University to be publicly defended on Friday 31 March 2023 at 13.00 in Magnélisalen, Kemiska övningslaboratoriet, Svante Arrhenius väg 16 B.

Abstract

This thesis summarizes a study on the pressure-induced amorphization (PIA) and structures of amorphous states of clathrate hydrates (CHs).

PIA involves the transition of a crystalline material into an amorphous solid in response of mechanical compression at temperatures well below the melting point. The first material observed to undergo PIA was hexagonal ice. More recently it was shown that compounds of water undergo the same phenomenon without decomposition, despite the presence of solutes. CHs, which are crystalline inclusion compounds consisting of water molecules encaging small guest species, undergo PIA at ca. 1–4 GPa below 145 K. The obtained amorphous CH phase can be further densified on isobaric heating at high pressure. This annealing step enables to retain an amorphous material on pressure release. There has been a significant amount of studies into the understanding of the nature of PIA and transformations between amorphous phases of pure ice. The aim of this thesis has been the understanding of the PIA in CHs and its relation to pure ice. New information on the nature of PIA and subsequent amorphous-amorphous transitions in CH systems were gained from structural studies and *in situ* neutron diffraction played pivotal role due to the sensitivity of neutrons to the light element hydrogen. Here a generalized understanding of the PIA in CHs and a clear image of amorphous CH structures are presented.

Keywords: *Clathrate Hydrates, Pressure-Induced Amorphization, Amorphous States, Glassy States, Ice, Neutron Diffraction.*

Stockholm 2023
http://urn.kb.se/resolve?urn=urn:nbn:se:su:diva-214449

ISBN 978-91-8014-186-4
ISBN 978-91-8014-187-1

Department of Materials and Environmental Chemistry (MMK)

Stockholm University, 106 91 Stockholm

PRESSURE-INDUCED AMORPHIZATION AND DISTINCT AMORPHOUS STATES OF CLATHRATE HYDRATES

Paulo H. B. Brant Carvalho

Stockholm
University

Pressure-Induced Amorphization and Distinct Amorphous States of Clathrate Hydrates

Paulo H. B. Brant Carvalho

ISBN print 978-91-8014-186-4
ISBN PDF 978-91-8014-187-1

Cover image: Baulot, I. (1702) Mutus Liber. Retrieved from the Library of Congress, https://www.loc.gov/item/10018432/. Permission under the Fair use law.

Printed in Sweden by Universitetsservice US-AB, Stockholm 2023

"In hindsight everything is much clearer. We should always look at things in hindsight, from the very beginning."

- Jekabs Grins

Doctoral Thesis 2023
Department of Materials and Environmental Chemistry

Faculty Opponent:
Doc. John Loveday
School of Physics and Astronomy
The University of Edinburgh, United Kingdom

Evaluation Committee:
Doc. Anita Zeidler
Department of Physics
University of Bath,United Kingdom

Prof. Lars G.M. Pettersson
Department of Physics
Stockholm University, Sweden

Doc. Martin Månsson
Department of Materials and Nanophysics
KTH Royal Institute of Technology, Sweden

Substitute:
Doc. Andrew Ken Inge
Department of Materials and Environmental Chemistry
Stockholm University, Sweden

Abstract

This thesis summarizes a study on the pressure-induced amorphization (PIA) and structures of amorphous states of clathrate hydrates (CHs).

PIA involves the transition of a crystalline material into an amorphous solid in response of mechanical compression at temperatures well below the melting point. The first material observed to undergo PIA was hexagonal ice. More recently it was shown that compounds of water undergo the same phenomenon without decomposition, despite the presence of solutes. CHs, which are crystalline inclusion compounds consisting of water molecules encaging small guest species, undergo PIA at ca. 1–4 GPa below 145 K. The obtained amorphous CH phase can be further densified on isobaric heating at high pressure. This annealing step enables to retain an amorphous material on pressure release. There has been a significant amount of studies into the understanding of the nature of PIA and transformations between amorphous phases of pure ice. The aim of this thesis has been the understanding of the PIA in CHs and its relation to pure ice. New information on the nature of PIA and subsequent amorphous-amorphous transitions in CH systems were gained from structural studies and *in situ* neutron diffraction played pivotal role due to the sensitivity of neutrons to the light element hydrogen. Here a generalized understanding of the PIA in CHs and a clear image of amorphous CH structures are presented.

Keywords
Clathrate Hydrates, Pressure-Induced Amorphization, Amorphous States, Glassy States, Ice, Neutron Diffraction

Sammanfattning

Denna avhandling sammanfattar en studie om tryckinducerad amorfisering (TIA) av klatrathydrater (KH), samt strukturer av amorfa tillstånd där av.

TIA är övergången av ett kristallint material till ett amorft fast ämne som svar på mekanisk kompression vid temperaturer långt under smältpunkten. Det första materialet som observerades genomgå TIA var hexagonal is. Därefter har det visat sig att det finns strukturer av vatten som trots närvaron av lösta ämnen genomgår samma fenomen utan att strukturen bryts ned. KH:er är kristallina inneslutningskomplex som består av ett gitter av vattenmolekyler, vilka omsluter små gästmolekyler. Dessa strukturer genomgår TIA vid ca. 1–4 GPa vid temperaturer under 145 K. Den erhållna amorfa KH-fasen kan förtätas ytterligare vid isobarisk uppvärmning under högt tryck. Detta steg gör det möjligt att behålla ett amorft material vid tryckavlastning. Det har gjorts en betydande mängd studier av TIA:s natur och omvandlingar mellan amorfa faser av ren is. Syftet med denna avhandling har varit att förstå TIA i KH:er och dess relation till ren is. Ny information om karaktären hos TIA och efterföljande amorfa-amorfa övergångar i KH-system erhölls från strukturella studier, där *in situ* neutrondiffraktion spelade en avgörande roll tack vare neutronernas känslighet för det lätta elementet väte. Utifrån detta arbete presenteras här en generaliserad förståelse av TIA i KH samt en tydlig bild av amorfa KH-strukturer.

Nyckelord
Klatrathydrater, Tryckinducerad Amorfisering, Amorfa tillstånd, Glasartade tillstånd, Is, Neutrondiffraktion

List of appended papers

This dissertation is based on the following papers, referred to in the text by their Roman numerals.

PAPER: I **Elucidating the guest disorder in structure II argon hydrate – A neutron diffraction isotopic substitution study**
P.H.B. Brant Carvalho, A. Mace, O. Andersson, C.A. Tulk, J.J. Molaison, and U. Häussermann, *Journal of Solid State Chemistry*, **285**, 121220 (2020).
DOI: 10.1016/j.jssc.2020.121220

PAPER: II **Transitions in pressure-amorphized clathrate hydrates akin to those of amorphous ices**
O. Andersson, P.H.B. Brant Carvalho, Y.J. Hsu, U. Häussermann, *The Journal of Chemical Physics*, **151**, 014502 (2019).
DOI: 10.1063/1.5096981

PAPER: III **Elucidation of the pressure induced amorphization of tetrahydrofuran clathrate hydrate**
P.H.B. Brant Carvalho, A. Mace, C.L. Bull, N.P. Funnell, C.A. Tulk, O. Andersson, and U. Häussermann, *The Journal of Chemical Physics*, **150**, 204506 (2019).
DOI: 10.1063/1.5083958

PAPER: IV **Pressure-induced amorphization of noble gas clathrate hydrates**
P.H.B. Brant Carvalho, A. Mace, O. Andersson, C.A. Tulk, J.J. Molaison, A.P. Lyubartsev, I.M. Nangoi, A.A. Leitão, and U. Häussermann, *Physical Review B*, **103, 6**, 064205 (2021).
DOI: 10.1103/PhysRevB.103.064205

PAPER: V **Exploring High-Pressure Transformations in Low-Z (H_2, Ne) Hydrates at Low Temperatures**
P.H.B. Brant Carvalho, A. Mace, I.M. Nangoi, A.A. Leitão, C.A. Tulk, J.J. Molaison, O. Andersson, A.P. Lyubartsev, and U. Häussermann, *Crystals*, **12 (1)**, 9 (2022).
DOI: 10.3390/cryst12010009

PAPER: VI **Structural investigation of three distinct amorphous forms of Ar hydrate**
P.H.B. Brant Carvalho, PIR Moraes, A.A. Leitão, O. Andersson, C.A. Tulk, J.J. Molaison, A.P. Lyubartsev, and U. Häussermann, *RSC Advances*, **11 (49)**, 30744-30754 (2021).
DOI: 10.1039/D1RA05697B

PAPER: VII **Neutron scattering study of polyamorphic THF $\cdot$ $(H_2O)_{17}$ – toward a generalized picture of amorphous states and structures derived from clathrate hydrates**
P.H.B. Brant Carvalho, M. Ivanov, O. Andersson, T. Loerting, M. Bauer, C.A. Tulk, B. Haberl, L.L. Daemen, J.J. Molaison, K. Amann-Winkel, A.P. Lyubartsev, C. L. Bull, N. P. Funnell, and U. Häussermann.
In manuscript

PAPER: VIII **Evidence Suggesting Kinetic Unfreezing of Water Mobility in Two Distinct Processes in Pressure-Amorphized Clathrate Hydrates**
O. Andersson, P.H.B. Brant Carvalho, U. Häussermann, Y.J. Hsu, *Phys. Chem. Chem. Phys.*, **24**, 20064-20072 (2022).
DOI: 10.1039/D2CP01993K

Reprints were made with permission from the publishers.

Contents

1 Introduction **1**

1.1 Clathrate Hydrates . . . 1
1.2 Clathrate Systems and Structures . . . 3
1.3 Clathrate Hydrates at High Pressures . . . 9
1.4 Amorphous States of Clathrate Hydrates . . . 11
1.5 Selection of Systems Studied . . . 12
1.5.1 Clathrate hydrates of noble gases . . . 12
1.5.2 Water-rich clathrate hydrates . . . 13
1.5.3 Low-Z clathrate hydrates . . . 13
1.6 Scope of this Thesis . . . 14

2 Neutron Scattering **17**

2.1 Neutrons as Elementary Particles . . . 17
2.2 Neutron Production . . . 18
2.2.1 Natural neutron sources . . . 18
2.2.2 Radioisotope sources . . . 18
2.2.3 Nuclear reactors . . . 18
2.2.4 Spallation sources . . . 19
2.3 Neutrons for Research . . . 20
2.3.1 Neutron moderation . . . 21
2.3.2 Time-of-flight neutron count . . . 22
2.4 Nuclear Scattering . . . 22
2.4.1 The scattering process . . . 23
2.4.2 Cross-section . . . 23
2.4.3 Scattering length . . . 23
2.4.4 Elastic scattering . . . 25
2.4.5 Inelastic scattering . . . 27
2.4.6 Coherent and incoherent scattering . . . 27

3 Sample Environment **29**
3.1 High Pressure . . . 29
3.2 Low Temperature . . . 30
3.3 Gas Pressure Cells . . . 30
3.4 Piston Cylinder and Clamp Cells . . . 31
3.5 Paris-Edinburgh Press . . . 33
3.6 High-Pressure Neutron Diffraction . . . 36
3.6.1 PEARL . . . 36
3.6.2 SNAP . . . 36
3.7 Molecular Dynamics . . . 39

4 Crystalline Clathrate Hydrates **41**
4.1 Synthesis . . . 41
4.1.1 THF- and other water-rich CHs . . . 42
4.1.2 Ar- and Xe-CHs . . . 42
4.1.3 H_2- and Ne-CHs . . . 43
4.2 Guest Disorder in CS-II Ar-CH . . . 45

5 Pressure-Induced Amorphization of Clathrate Hydrates **49**
5.1 Background . . . 49
5.2 PIA of Water-Rich CHs . . . 51
5.3 PIA of Ng-CHs . . . 54
5.4 LT Compression of Low-Z CHs . . . 60
5.5 Summary . . . 62

6 Distinct Structures of Amorphous CHs **63**
6.1 Background . . . 64
6.2 Three Distinct Amorphous Forms of Ar-CH . . . 65
6.3 Distinct Amorphous Forms of THF-CH . . . 71
6.4 Glass Transitions in Pressure-Amorphized CHs . . . 73

7 Summary and Prospects **75**

Nomenclature

CH	Clathrate Hydrate
EoS	Equation of State
ESS	European Spallation Source
HDA	High Density Amorphous
HP	High Pressure
INS	Inelastic Neutron Scattering
LDA	Low Density Amorphous
Linac	Linear Accelerator
LT	Low Temperature
MD	Molecular Dynamics
ND	Neutron Diffraction
Ng	Noble Gas
NMR	Nuclear Magnetic Resonance
NPD	Neutron Powder Diffraction
NTP	Normal Conditions of Temperature and Pressure
ORNL	Oak Ridge National Laboratory
PDF	Pair Distribution Function
PEC	Paris-Edinburgh Cell
RA	Recovered Amorphous

RDF	Radial Distribution Function
SNS	Spallation Neutron Source
THF	Tetrahydrofuran
TOF	Time-of-flight
VHDA	Very High Density Amorphous
XRD	X-ray Diffraction

1

Introduction

1.1 Clathrate Hydrates

Clathrate hydrates (CHs) are inclusion compounds of water and small, typically apolar, guest species. Guests are rather diverse in nature and cover a variety of chemical functionalities, but commonly CHs form with gases or volatile liquids. There is a plethora of suitable CH-former species such as noble gas atoms, diatomic molecular gases (e.g., H_2, O_2 and N_2), linear and bent triatomic molecules (e.g., CO_2 and H_2S) and larger molecules such as tetrahydrofuran (THF) and SF_6 [see Sloan Jr. and Koh [1], Alavi and Ripmeester [2] and references therein].

CHs crystallize in environments where water and guest species coexist at low temperature and pressurized atmosphere. The first CH synthesis was reported by Sir H. Davy in 1811 [3], when he worked with chlorine gas and discovered that it forms a CH with water ($Cl_2 \cdot \sim 6\,H_2O$). CHs form naturally and abundantly with gaseous guests, such as CH_4 and CO_2 at the bottom of oceans, deep lakes, or in permafrost regions. Large CH deposits are known to be present in these environments [4, 5]. CHs may also exist in outer space, in many solar system bodies such as in Martian permafrost, on the surface of Titan and other satellites [6] and possibly even in the interstellar medium [7].

The amount of gas species that may be entrapped in crystalline CH is remarkable, reaching potentially over 30 mol% [8], which represents an outstanding storage capacity. Gas hydrates – a nomenclature often used to designate CHs of gaseous guests – are particularly relevant since CH storage capacity is several orders of magnitude higher than the solubility of hydrophobic gases in liquid water. For this reason, gas

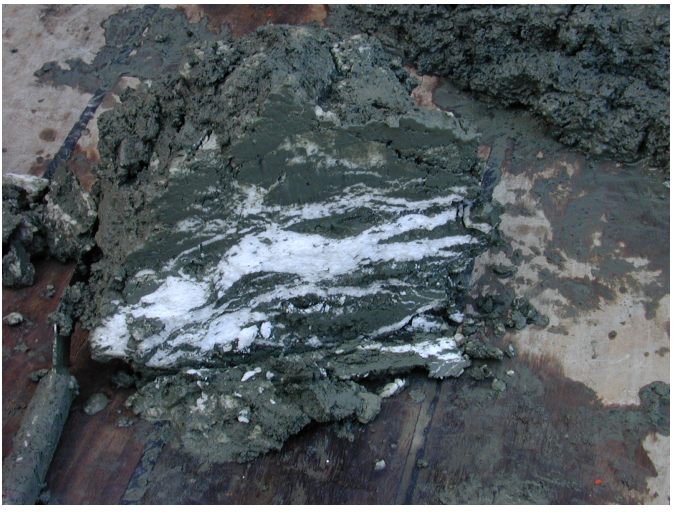

Figure 1.1.1: Methane CH embedded in sediment. Material found during a research cruise with the German research ship FS SONNE in a depth of about 1200 m. The clathrate hydrate (white) has been deposited in layers into the sediment. Extract from https://www.mindat.org/min-46016, access on 2022-12-23, permission under the Fair use law.

hydrates have a tremendous potential in energy storage and transportation applications.

The environmental relevance of naturally forming CHs was widely recognized after the Deepwater Horizon oil spill disaster in the Gulf of Mexico, 2010. Natural gas CHs can form in underwater gasoducts due to pressure and low temperatures, leading to plugging of the pipelines [9]. In fact, natural gas molecules are generally good CH formers. It is estimated that the amount of CO_2 and CH_4-bearing CHs in marine sediments on Earth (see picture in Figure 1.1.1) is twice as abundant as all other fossil fuel sources combined [10]. The abundance of greenhouse gases trapped in natural CHs significantly aggravates climate change. It is suggested, for instance, that CHs on the seabed could be an important component of a slow global warming feedback loop. Small increases in global temperature could destabilize CH formation and release the trapped greenhouse gases, further exacerbating climate change [11].

CH science is very active in the fuel industry, having gas capture, storage, and energy-related applications due to their large storage capacity in a clean material (ice) and abundance in nature [10]. CHs of natural gas have been drawing particular attention as energy source. CHs containing H_2 are also envisaged as a promising technology for fuel cells [8]. Further, there have been suggestions of alternative applications for CHs as for

example advanced drug delivery [12], water desalination [13], separation of ionic liquids [14], and there is much interest in CHs for fundamental science.

1.2 Clathrate Systems and Structures

Clathrates (from the Latin word *clathratus* referring to cages [15]) are combinations of substances in which the major component, the host, encages individual species of the minor compound, the guest. With water as host, the resulting systems are thus named clathrate hydrates. Substances are associated through weak chemical interactions, which are most commonly of van der Waals type. Although little interacting, guests play important stabilizing role in CHs since the empty clathrate structures are thermodynamically unstable [16]. CHs are termed "canonical" when guests are either atomic or molecular (as opposed to ionic species) and when there is no permanent hydrogen bond with water molecules of the hosting clathrate structure.

Hydrogen-bonding guests, such as molecules with alcohol, ether, ketone and amine functional groups, can also form CHs. These species are often soluble due to hydrogen bonding with the water solvent, and many readily crystallize as CH upon cooling. Nevertheless, hydrogen bonds introduce a destabilizing effect to the clathrate framework [17]. Strongly bonding molecules such as methanol act as clathrate inhibitors rather than CH-formers, so only short-lived hydrogen bonds are found in crystalline canonical CHs.

The clathrate framework of water molecules is distinct from common ice (called hexagonal ice or ice I_h, Figure 1.2.1(a)). Both water and guest molecules are long-range ordered. Water molecules in the surroundings of guest species – the hydration shell of a guest – form polyhedral cages (as illustrated in Figure 1.2.1(b)) which vary in size and geometry depending on the size and nature of the guest. As a result, there are various crystalline clathrate structures that may be realized.

Guest sizes appropriate for CH formation are in a range ca. 3–6 Å. Smaller guests, e.g., He, can effuse from the water framework. Larger guests will require too-large cages for a stable clathrate structure.

Cage boundaries correspond to polygonal rings of water molecules. The bond angle $\angle$HOH $\approx 109.5°$ in the tetrahedral environment of water molecules is much closer to the angles in a regular pentagon (108°) than in a hexagon (120°), so the pentagon is the most stable ring formed by hydrogen-bonded water molecules. Rings of water molecules join to form three-dimensional frameworks, and the most common polyhedral cage formed is the 20-vertex pentagonal dodecahedron (D-cage or 5^{12}). Because of the 5-fold symmetry of pentagonal faces in such type of cage, frameworks based on 5^{12}

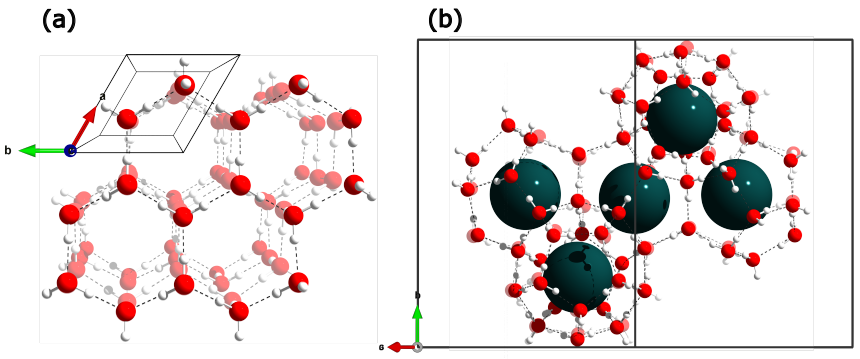

Figure 1.2.1: (a) Hexagonal lattice structure of typical ice (I_h). (b) Cage structures hosting guests on a clathrate lattice (cubic structure II).

cannot fill space and consequently larger cages containing hexagonal faces are generated [18].

Despite the numerous structures that may form, the majority of CHs crystallize with two main crystallographic types of cubic arrangements [19]. In the so-called cubic structure I (CS-I) with space group $Pm\bar{3}n$, the larger cages are generated with two hexagonal faces forming 24-vertex tetrakaidecahedra, T-cages or $5^{12}6^2$. In the cubic structure II (CS-II), space group $Fd\bar{3}m$, larger cages are generated with four hexagonal faces forming 28-vertex hexakaidecahedra, H-cages or $5^{12}6^4$. The structures of CS-I and CS-II, and D, T, and H cages are shown in Figure 1.2.2. Geometrical properties of CH structures are summarized in Table 1.1.

In either clathrates CS-I and CS-II, water molecules are tetrahedrally coordinated. The four hydrogen sites surrounding oxygen atoms from water molecules are equally probable to represent either a regular bond (which assumes a hydrogen-bond donor role to a coordinating H_2O molecule) or a hydrogen bond to a coordinating H_2O molecule (by which O functions as hydrogen-bond acceptor). Hydrogen bonds and orientations are constrained by the so-called Bernal-Fowler ice rules [20]: (1) each oxygen participates in four hydrogen bonds, twice as donor and twice as acceptor; (2)

molecules are oriented in such a way that only one hydrogen atom lies between each pair of oxygens; and (3) there is no preferred configuration, i.e., all orientations are equally probable with no net polarization. As a result, the orientation of hydrogen atoms in CH structures is disordered, similar to that in most ices.

To observe the local connectivity, it is common to build up models of the pair distribution functions (PDF) of atoms. These functions $\mathrm{g}(r)$ give the probability of finding the center of any atom between distances r and $r + \mathrm{d}r$ from the center of a given atom [20]. Figure 1.2.3(a) shows a PDF representation of the ice structure in Figure 1.2.1(a). The shaded areas are guides to visualize the distinct coordination shells, which appear as peaks in PDFs. Figure 1.2.3(b) shows the analogous water-oxygen (Ow) PDF in a CH structure, as well as the Ow-guest PDF. Note how the local water environment (at short values of r) is similar in both structures, but long-range ordering (long values of r) changes as a result of the guest inclusion.

The presence of guests in the ice scaffolding disrupts the hydrogen-bonded network of water molecules through volume exclusion (cf. Figure 1.2.3) but doesn't interrupt it. The connectivity of the water network is reestablished around the solute species leading to cages. Guests coordinate to 20–28 water molecules, rendering each interaction very weak, and guests are generally located at the center of cages or distributed within the cage in a near-spherical manner [21].

The properties and flexibility of hydrogen bonds are responsible for most of the macroscopic properties of CHs. It is then not surprising that many of such properties are similar to those of pure ice. A notably exceptional property of CHs is their glass-like thermal conductivity [22], which might relate to the large unit cells or the motion of guests within cages. Although paramount for the structural integrity of CHs, guest interactions with the hosting ice structure are not strong enough to significantly alter macroscopic properties [23].

Each CS-I unit cell (a $\approx$ 11 Å) contains two small and six large cages, here represented with the formula $(2\,\mathrm{D} + 6\,\mathrm{T}) \cdot 46\,\mathrm{H_2O}$. CS-II unit cells are larger (a $\approx$ 17 Å) and composed of $(16\,\mathrm{D} + 8\,\mathrm{H}) \cdot 136\,\mathrm{H_2O}$. Cage geometries are described in Table 1.2. In the fully occupied scenario, CS-I is composed of one guest (G) for every 5.75 molecules of water (represented as 1:5.75 or $\mathrm{G} \cdot 5.75\,\mathrm{H_2O}$). The composition of fully occupied CS-II is $\mathrm{G} \cdot 5.6\,\bar{7}\,\mathrm{H_2O}$.

Clathrate cages are typically not fully or evenly occupied so CHs are non-stoichiometric compounds. In both CS-I and CS-II, small (D) and large (T or H) cages are normally occupied to 80–90%, leading to an average CH guest composition of $\mathrm{G} \cdot \sim\!6\,\mathrm{H_2O}$ as, e.g., in the chlorine CH. Multiple occupancy of cages is also rarely observed and when only with very small-sized guests. The average cavity diameters

Table 1.1: Geometrical and crystallographic parameters of cubic clathrate hydrate structures

Clathrate structure	Unit cell content Space group	Unit cell parameter	Cages	Symmetry of cage centers
CS-I	(2D+6T) · $46H_2O$ $Pm\bar{3}n$	a ≈ 11 Å	5^{12} (D) $5^{12}6^2$ (T)	m3 $\bar{4}$2m
CS-II	(16D+8H) · $136H_2O$ $Fd\bar{3}m$	a ≈ 17 Å	5^{12} (D) $5^{12}6^4$ (H)	3m or $\bar{3}$m $\bar{4}$3m

Table 1.2: Geometry of clathrate hydrate cages

CH crystal structure	CS-I		CS-II	
	Small (D) cages	Large (T) cages	Small (D) cages	Large (H) cages
Polyhedral description	5^{12}	$5^{12}6^2$	5^{12}	$5^{12}6^4$
Number of cages per unit cell	2	6	16	8
Average available radius	2.5 Å	2.9 Å	2.5 Å	3.3 Å
Number of water molecules	20	24	20	28

(twice the average distance of oxygen atoms from the center of the cage) in cubic CH structures are 7.8 Å in D-cages, 8.6 Å in T-cages and 9.4 Å in H-cages [2]. Considering the van der Waals diameter of a water molecule (2.8 Å [24]), the open spaces that guests may occupy in D, T and H cages are only 5.0 Å, 5.8 Å and 6.6 Å, respectively.

CS-I forms with medium-sized guests such as CH_4 and Xe. CHs with guests that are ca. 6 Å wide crystallize with the CS-II because they can only fit in the larger H cages, while D cages remain empty or may be filled by smaller co-guests. This is the case of CHs with THF and SF_6 where H cages are 100% filled. CS-II also occurs for smaller species, N_2, H_2, O_2 and most noble gases, with both types of cages not fully occupied. It is presumed that smaller guest species occupy preferentially smaller cages, which are more common in CS-II than in CS-I [25]. Guest dynamics within the larger H cages may have also a stabilizing role [26]. In the case of the very small guests H_2, He and Ne, multiple occupancy of H cages has been verified and up to 4 guests can be found within H cages. Multiple occupancy of H cages in CS-II can thus lead to the guest-rich compositions of up to $G \cdot 2.8\bar{3}\,H_2O$, rendering, e.g., H_2-CH a promising storage material in the prospective of a hydrogen-based economy.

As a consequence of the flexibility of hydrogen bonds and the weak intermolecular forces, temperature and pressure significantly affect the structural properties of CHs. Especially changing the density through the application of external pressure is a valuable tool to probe intermolecular interaction potentials. The behaviour and properties of CHs further deviate from that of pure ice with increasing guest fraction, lower temperatures and higher pressures, as guest-host interactions (i.e., interatomic and intermolecular forces) become more important [16].

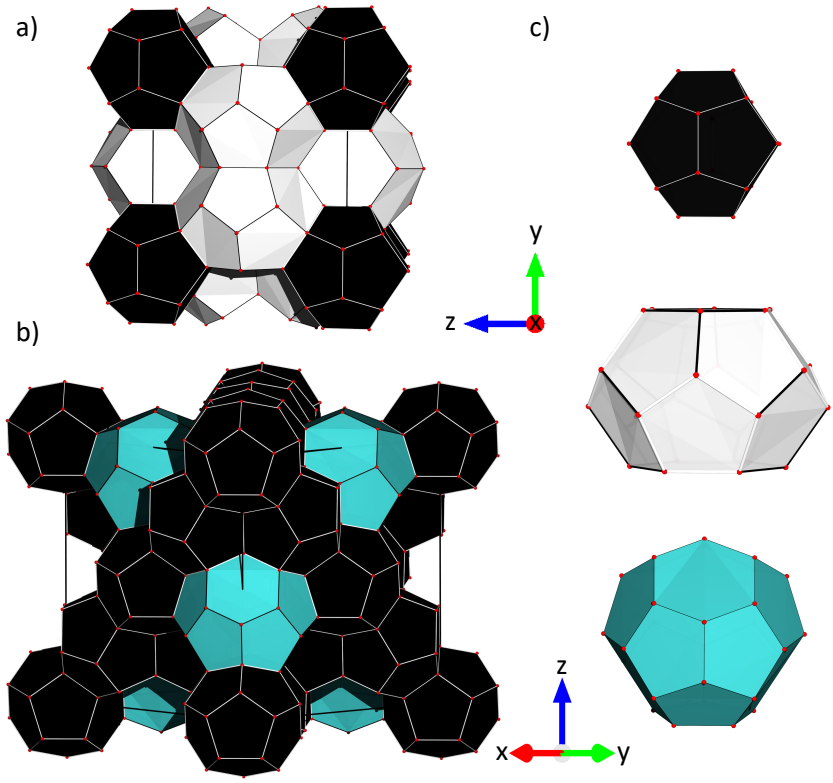

Figure 1.2.2: Unit cell of the cubic clathrate hydrate structures. (a) Cubic structure I; (b) cubic structure II; and (c) cages generated by the framework of water molecules. From the top: dodecahedral (D) cage, tetrakaidekahedral (T) cage, and hexacaidecahedral (H) cage. Extract from Paper IV.

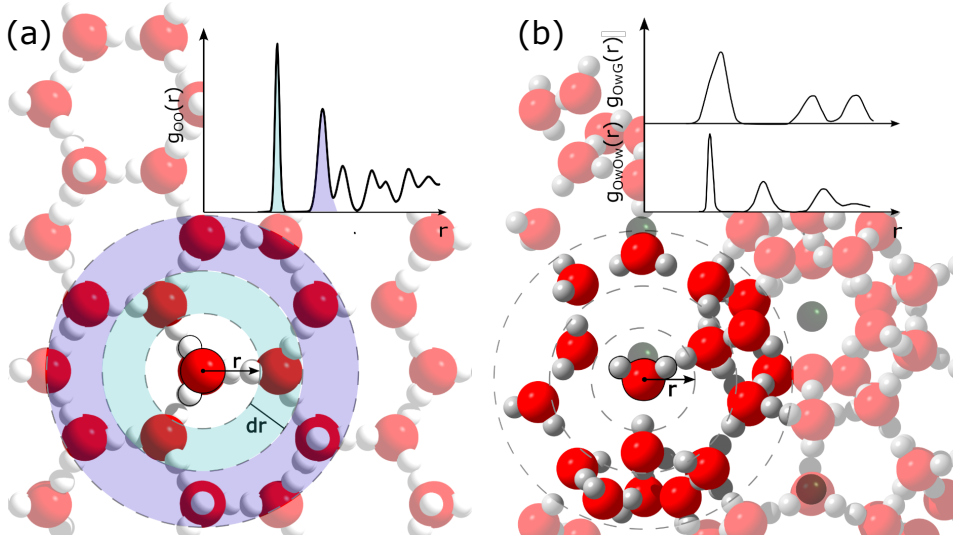

Figure 1.2.3: (a) Local structure of hexagonal ice represented as a pair distribution function of oxygen pairs, $\mathrm{g_{OO}}(r)$. Areas underneath peaks in the PDF function are also visualized in the crystalline structure centered at one arbitrary water molecule. (b) Local structure of a clathrate hydrate (cubic structure II with guests occupying both kinds of cages) represented as water oxygen pairs, $\mathrm{g_{OwOw}}(r)$, and water oxygen-guest pairs, $\mathrm{g_{OwG}}(r)$.

1.3 Clathrate Hydrates at High Pressures

There is considerable interest in the changes CHs undergo under pressure [16]. When put under compression, CHs will contract in volume, suffer deformation and the result could vary. The CH may remain stable and the cage structures and guests will be compressed up to their limits. The CH could dissociate, releasing its guest species and leaving behind water-ice structures. It is also possible that the hydrate structure changes.

The pressure behaviour of (pure) ice is well documented and helps us understand the many anomalies in solid and liquid water [22]. Pure water has a spectrum of solid phases, the vast majority resulting from the application of pressure. These phases have different crystal structures, densities, and properties than the more common low-pressure forms of ice.

Pressure transformations of CHs are not as well studied, although they can be another gateway to understanding water properties. The specific outcome that occurs depends on the guest species, composition, pressure, temperature, and this relationship is still not fully understood.

At very high pressures — in the gigapascal (GPa) regime (note that 1 GPa = 10 kbar) — and near room temperature, CHs undergo structural transitions to denser hydrate phases and filled ice structures (FIS, non-clathrate inclusion compounds). For example, the binary system Ar:H_2O initially forms a CS-II phase at slightly elevated pressure (a few hundred bars) near room temperature. When further compressed, Ar:H_2O transforms into differently-structured clathrate phases: at 4.6 kbar a hexagonal structure (HS-III) is formed, which is superseded by a tetragonal phase (TS-I) at 7.7 kbar [27]. In both HS-III and TS-I multiple argon atoms occupy very large cages stabilized by pressure. Lastly, above 21 kbar Ar:H_2O assumes a FIS phase analogous to the ice I_h framework. At pressures higher than 61 kbar the FIS phase decomposes into solid Ar and ice VII [28]. The Ar:H_2O composition varies between each phase [29], and high-pressure CH phases are typically more guest-rich.

The result of compression of different CHs can vary depending on the specific type of CH and the guest species that is included in the structure. CH_4:H_2O forms a CS-I phase at slightly elevated pressure near room temperature. Upon compression, it transforms into a HS-III clathrate stable to very high pressures, before eventually being superseded by a FIS similar to the ice I_h structure [30]. Different CHs can attain unique crystal structures and different bonding interactions between the water molecules and the guest, which can affect their stability and behavior under high pressures. Figure 1.3.1 summarizes the phase transformations for a selection of CHs. Furthermore, contrary to the expectation that hydrates should always decompose with pressure,

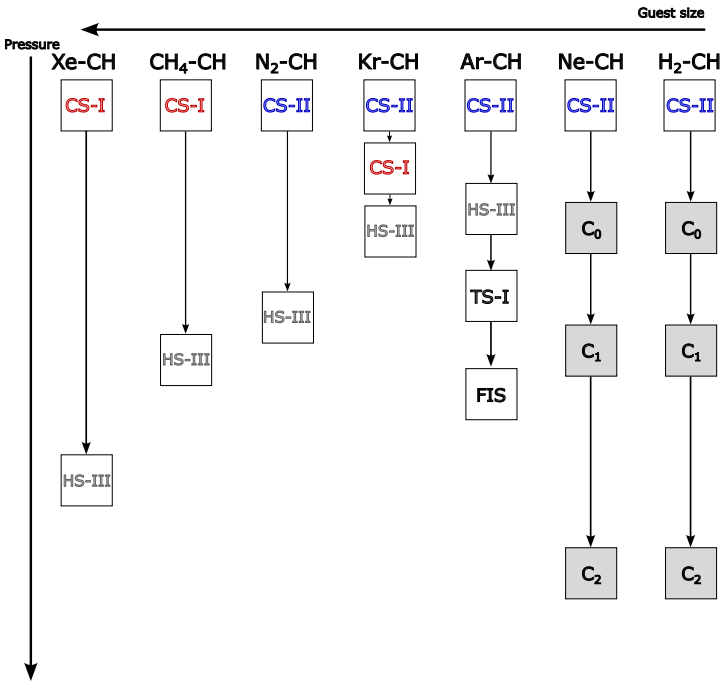

Figure 1.3.1: Phase behaviour of some clathrate hydrates with pressure at (or near) room temperature. Adapted from Ranieri [32].

CH_4:H_2O and H_2:H_2O were found to form FIS phases stable up to extremely high (Mbar) pressures when compressed at room temperature [31].

From the several phases of ice and inclusion compounds that form under high pressure, many of them can be quenched at liquid nitrogen (LN_2) temperature allowing a recovery to atmospheric pressure without resulting in any phase transition. At low temperatures, atoms will move more slowly, which can make it more difficult for them to re-arrange into a crystal structure.

Conversely, at low temperatures pressure-induced crystal-crystal phase transitions of ice and CHs are suppressed and instead collapse of the crystal structure into an amorphous solid is observed. This phenomenon is called pressure-induced amorphization (PIA) [33].

1.4 Amorphous States of Clathrate Hydrates

PIA is known to happen in several materials, most importantly water-ice. Ice I_h collapses to an amorphous state, termed high-density amorphous ice (HDA), on pressurization to 10 kbar at 77 K [33]. From HDA, further, distinct amorphous states can be obtained. On depressurization in the 125–140 K range HDA transforms to low-density amorphous ice (LDA) [34], and on heat-cycling to ca. 170 K near 10 kbar HDA transforms into very-high-density amorphous ice (VHDA) [35]. The existence of several different amorphous configurations is termed polyamorphism [36, 37].

Amorphous solids resemble liquids in having no long-range order, but they differ from liquids for being frozen in a given structural arrangement. Because PIA leads to a material structurally like a liquid, originally, the PIA of ice was referred to as a pressure-induced melting, i.e., the amorphous state HDA would be related to a liquid or a glass dependent on its glass transition temperature. It was later noticed that the amorphization pressure well exceeded that of the (extrapolated) equilibrium melting curve and simulations suggested that the process was instead due to (non-equilibrium) mechanical collapse of the crystalline structure. The nature of PIA and amorphous ices is still discussed. PIA and polyamorphism have now been observed in other materials, e.g., silica [38].

Polyamorphism implies that the amorphous configurations are distinctly different. Although amorphous ices are often treated as though they are homogeneous, this is not inherently true. Amorphous phases may, for instance, be composed of several density spots and even nano- or micro-crystalline domains. Due to a lack of dynamic equilibrium between all possible configurations of the molecules in this arrested liquid, amorphous solids are known for having different properties when produced in different ways, in contrast to a liquid. Amorphous states can undergo relaxation and change continuously, producing "substates" of the same amorphous state. Distinct amorphous states can be reversibly interconverted and show hysteresis upon a first-order-like transition [39].

Despite the significant structural differences, CHs behave similar to pure ice when compressed at low temperatures and undergo PIA and subsequent amorphous-amorphous transitions. PIA involves displacement of guest molecules from their cage-like structure and results of the breaking of the hydrogen bonds between water molecules. The process accompanies changes in volume, density, and other properties important for CHs. Exploring PIA and phase boundaries in CHs are important steps towards an understanding of the crystallization process. Structural studies are also valuable to understand the stability of CH phases with respect to the presence and nature of the guests entrapped in it.

Such studies at extreme conditions of pressure are limited by technical challenges, even more so in simultaneous high-pressure, low-temperature experiments. Yet, they offer novel insights in the search for better and cleaner energy storage strategies as well as proxy systems to study water properties otherwise inaccessible.

1.5 Selection of Systems Studied

There are several types of CHs that are of interest to study at high pressure. The CHs chosen for this thesis work were considered model systems for canonical CH with a single guest species and include CHs with noble gas guests, CHs with water-rich composition, and CHs with low-Z guests.

1.5.1 Clathrate hydrates of noble gases

The monoatomic noble gases (Ngs) from Ne to Rn are known to form CHs. Ne-, Ar-, and Kr-CH crystallize as CS-II, whereas Xe- and Rn-CH adopt CS-I. Helium does not form CHs, but He inclusion in hydrate structures (filled-ices I_h and II) were reported at high pressures [40]. Nevertheless, He-CH can still be obtained by filling ice XVI (an emptied clathrate structure obtained by evacuating CS-II H_2- or Ne-CH) at around 100 K [40].

Ng-CHs will not form near atmospheric pressure because of the low solubility and low reactivity of the Ng. They can be produce in laboratory conditions at high pressures. After synthesis, Ng-CHs can be recovered and kept stably at LN_2 temperature. Except for Ne-CH, their composition is $Ng \cdot \sim 6H_2O$ with cages 80–90% filled.

The Ng species have dimensions of a few Ångstroms, are spherical and little interacting. Guest-host interactions are isotropic, which makes modelling of such system simple and reliable. Consequently, Ng-CHs represent ideal prototypical systems providing a homologous series of increasingly larger (and heavier) guests. Different Ngs also crystallize with different CH structures, which helps understand the preference relation of each structure type with the nature of the guest. The near room temperature high-pressure behaviour of Ng-CHs is well studied [16], but very few high-pressure, low-temperature studies are reported. Studies using Ng-CHs systematically addressed the effects of guest size and occupancy to the CH stability and throughout amorphization.

Studies with Ng-CHs were limited to Ne–Xe, prioritizing Ne, Ar and Xe in experiments.

1.5.2 Water-rich clathrate hydrates

THF, as well as other larger organic molecules, e.g., 1,3-dioxolane and cyclobutanone, all form CHs with the CS-II structure. Guest molecules are well miscible with water, so the corresponding CHs are easily obtained by cooling stoichiometric water solutions below the melting point, which is slightly above 0 °C at atmospheric pressure. Compositions are stoichiometric because of the preferential (100%) filling of only H cages. The fixed composition (1:17 or $G \cdot 17\,H_2O$) and the presence of empty cages make water-rich CHs distinct from other systems.

A selection of water-rich CHs and THF-CH in particular were investigated. THF-CH has been extensively investigated as a possible reduced-pressure alternative to the synthesis of gas-bearing hydrates for storage and transportation [41]. As opposed to Ng-CHs, larger organic molecules interact more with the hosting framework. In THF-CH, these interactions include the possibility of hydrogen-bond formation, which may induce peculiar dynamic behaviours and changed physical properties [42].

Because the mechanism of PIA involves filling unoccupied space in crystal structures, empty cages particularly present in water-rich CHs were also an important topic to address.

1.5.3 Low-Z clathrate hydrates

High molecular weight Ng atoms (Ar–Rn) form CHs at pressures less than 1 kbar. The low-Z species He, Ne and H_2 don't form CHs at these conditions. Ne is the second-smallest Ng after He. The synthesis of CS-II-type Ne-CH requires substantially higher pressures, 2–3 kbar, which is similar to CS-II H_2-CH [43].

Typically, a cage in a clathrate structure is only singly occupied. Rare cases of multiple occupancy have been observed at high pressures in CHs of gases with low molecular weight (low-Z). H_2-CH, for example, can host up to four H_2 molecules in the larger H cages of the CS-II, what leads to the much-increased guest composition as previously mentioned [8]. H_2- and Ne-CHs at full (multiple) occupancy can reach up $1{:}2.8\bar{3}$ composition. This represents an enormous potential in gas storage, especially for H_2. The main challenge is the current pressure requirement for the synthesis of low-Z CHs (described in more detail in Chapter 4). Once depressurized to atmospheric pressure, a fraction of the H_2 guest effuses from the ice framework to a recovered composition of ca. 1:4.25. This effusion, in the case of Ne-CH, is controversial due to the very few references available [44] but likely similar to H_2-CH.

The ability of small guests to hop through cages, diffuse and effuse from the ice framework even at low temperature is unique to low-Z guests, and it was exploited for example for the synthesis of ice XVI [44]. After that, two new ice structures have been

discovered also by emptying hydrates of low-Z guests: ice XVII from the Compound 0 (C_0) structure [45]; and cubic ice (I_c) without stacking disorder from the filled Compound 2 (C_2) structure [46].

Low-Z CHs have unique guest dynamics and phase behaviour near room temperature. Their pressure behaviour at low temperature was deemed to deviate from that of common guests.

1.6 Scope of this Thesis

The studies presented in this thesis examine the impact of various guests on the PIA of CHs. H_2-CH, Ng-CH, and large guests in water-rich CHs were all investigated as part of the effort to understand the properties and diversity of amorphous states of CHs. CHs offer a unique opportunity to study the poorly understood properties of water. This is explored to understand the analogy between the PIA of ice versus CHs.

The focus of this work is on three main topics:

- The structural characterization of crystalline CHs under high pressure and/or low temperature;
- The pressure-induced amorphization of CHs;
- The unique structures of distinct amorphous states of CHs.

Neutron scattering is a powerful technique in the study of hydrogen-rich compounds. Chapter 2 is dedicated to neutron scattering. Chapter 3 then introduces the appropriate tools used for sample environments, extreme condition neutron experiments and molecular modelling.

Chapter 4 introduces the synthesis of several crystalline CHs that were used in experiments. Neutron scattering experiments were particularly useful in exploring the crystalline CH structures. This is well exemplified in this chapter by the use of isotope substitution neutron diffraction to unveil the guest distribution within a clathrate structure (Paper I).

Chapter 5 presents a unified picture of the PIA behaviour of CHs. In Chapter 6 their various amorphous structures are analyzed and put in the context of pure water-ice. The results reported in this thesis present a comprehensive view of the temperature- and pressure-behaviour of CHs, as discussed in Papers II, III, IV and V. Subsequently a clear image of how the amorphous structures look like and their properties is presented in

Chapter 6, from the work in Papers VI, VII, and VIII.

2

Neutron Scattering

Neutron and X-ray scattering are the core of structural studies and atomistic modelling of ice and clathrates. Neutrons have a distinguished interaction with matter. This chapter presents a short introduction to neutron scattering with the fundamentals required to understand the pivotal role of neutron scattering, and particularly diffraction, in this work.

2.1 Neutrons as Elementary Particles

Neutrons are zero-charged subatomic particles with half-integer spin, mass m_n = 1.0087 a.u. and magnetic moment μ_n = -1.913 μ_N (nuclear magnetons) [47]. Together with protons, neutrons constitute the nucleus of atoms (nucleons). The *strong force* holding neutrons and protons together within nuclei is orders of magnitude stronger than electromagnetic (Coulomb) interactions. Therefore, the observation of free neutrons must be preceded by very energetic nuclear reactions.

The discovery of neutrons dates back to 1932 by Chadwick [48], who used the experiment of alpha particle ($^4_2\mathrm{He}^{2+}$) bombardment of beryllium to show that the outcome radiation were fast neutrons. The nuclear reaction in this experiment can be summarized as:

$$^9_4\mathrm{Be} + {}^4_2\mathrm{He}^{2+} \rightarrow [{}^{13}_6\mathrm{C}] \rightarrow {}^{12}_6\mathrm{C} + {}^1_0\mathrm{n}. \tag{2.1}$$

Free neutrons produced in nuclear reactions have a lifetime (τ_n) of 879.4(6) s, less than 15 minutes [47]. Upon (β-)decay, neutrons convert into a proton-electron pair plus

an electron neutrino:

$$\mathrm{n}^0 \rightarrow \mathrm{p}^+ + \mathrm{e}^- + \bar{\nu}_e. \tag{2.2}$$

2.2 Neutron Production

2.2.1 Natural neutron sources

Because free neutrons are rather short-lived, neutrons from cosmic sources cannot reach Earth. Natural atmospheric neutrons occur as secondary products of cosmic radiation, generated by high-energy collisions between cosmic protons and nuclei in the atmosphere. Moreover, this natural neutron production is a function of atmospheric depth, and the average thermal neutron flux at the surface of the Earth is around 10^{-4}–10^{-3} n/cm^{2}s (or more illustratively, an average of 10 atmospheric neutrons cross your body each second) [47]. Neutron production also occurs in natural nuclear reactors by the spontaneous fission of heavy elements present in the ground (e.g., $^{238}_{92}$U).

2.2.2 Radioisotope sources

Like the alpha particle bombardment of beryllium, there are several mixtures of radioisotopes (e.g., ^{210}Po, ^{226}Ra, ^{239}Pu, ^{241}Am) and light elements (e.g., Be, B, F) that produce neutrons. The mean energy produced in these reactions is of about 5 MeV per neutron produced, and the neutron yield is very inefficient. Radioisotope sources are used for instance in testing and development of neutron instruments.

2.2.3 Nuclear reactors

Neutron-induced nuclear fission is the core of all progress in nuclear technology, including research neutron facilities. Heavy nuclei can capture a neutron and subsequently break up into smaller nuclei. The process accompanies an enormous energy release, about 200 MeV per non-captured neutron, plus an efficient production of fast neutrons, a part of which is available for capture provoking a chain reaction. Enrico Fermi in 1942 demonstrated the first self-sustaining nuclear reaction in the Chicago Pile reactor CP-1 as part of the development of nuclear weapons, an effort during the Second World War known as the Manhattan project. Modern high-flux research reactors all consist of controlled self-sustaining reactors which operate on the nuclear fission principle. Because such reactions are extremely exothermic, heat transfer and dissipation is a limiting factor to scaling up neutron production in reactor sources. Although a lot more complex, the fission of uranium-235 can be exemplified as:

$$^{235}_{92}\mathrm{U} + ^{1}_{0}\mathrm{n} \rightarrow ^{141}_{56}\mathrm{Ba} + ^{92}_{36}\mathrm{Kr} + 3\,^{1}_{0}\mathrm{n} + \gamma + heat. \tag{2.3}$$

2.2.4 Spallation sources

The efficient production of neutrons is not restricted to nuclear fission. Victor Hess demonstrated that neutron sources in the atmosphere generated by cosmic rays operated by a different nuclear process called spallation [49]. When high-energy (in the GeV range) particles collide with nuclei, nucleons distribute the energy within the nucleus knocking out a few particles, among which neutrons. The "knocking-out" process is termed evaporation. The main product of the spallation process is neutrons. The leftover radioactive nuclei decay with emission of beta particles and γ-rays. Spallation generates an average of 30 MeV [47] energy released per neutron produced.

Spallation neutrons can be produced in laboratories equipped with particle accelerators. Spallation sources use most commonly synchrotrons, cyclic particle accelerators. In synchrotrons, charged particles are forced to travel a closed path by bending magnets.

Figure 2.2.1 presents a scheme of a spallation neutron source. Neutrons are produced in abundance from the collisions of high-energy particles with heavy metal targets (e.g., tungsten and mercury). An efficient (high-brilliance) production requires tightly bunched pulses which repeat at short time intervals arriving simultaneously at the target from the accelerator. With a constant particle production at the source, it is challenging to pile more particles in a beam without perturbing the motion of the particles already there. To solve this problem and increase the brilliance, accelerators pile up charged accelerated particles in synchrotron rings by first producing negatively charged (H^-) in a linear accelerator (Linac). Electrons from (H^-) are stripped off (typically by a carbon foil) before injection into the synchrotron. Accelerated proton beams generated this way are thus stacked in bunches, giving accelerator-based neutron sources a pulsed nature, as opposed to the continuous neutron production from nuclear reactors.

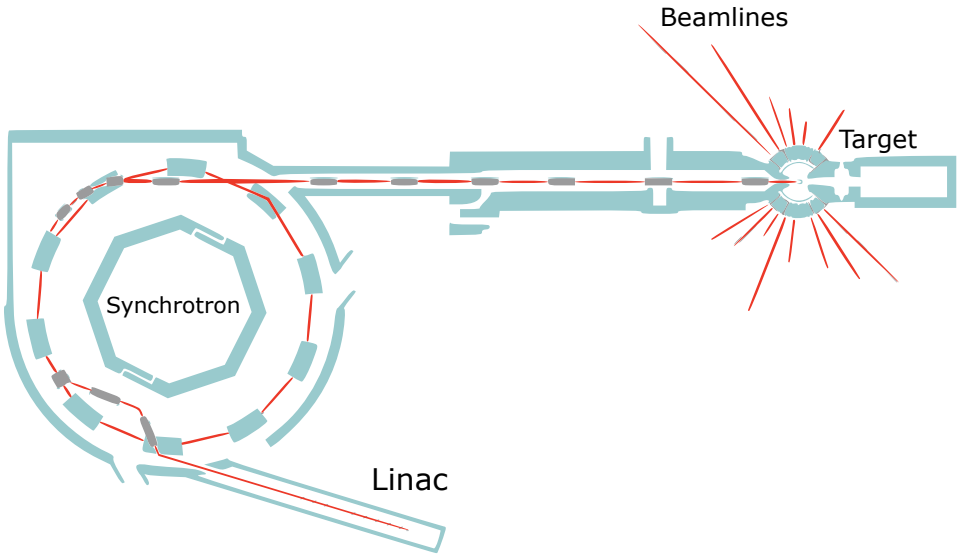

Figure 2.2.1: Scheme of a spallation neutron source. Adapted from http://pd.chem.ucl.ac.uk/pdnn/inst3/pulsed, access on 2023-01-06, permission under the Fair use law.

2.3 Neutrons for Research

Currently there are a few alternatives when it comes to neutron sources for research. Low-flux reactors, typically used for energy production, will spend the radioactive fuel over a time as long as possible. Research at low-flux sources usually only allow for testing and development. High-flux reactors and spallation sources play a dominant role for research.

To conduct research at neutron sources, cuts in the source shielding have to be made to clear out a neutron beam path, which is called a beamline. Beamlines consist of guides or flight tubes leading to end-stations. Beamlines aim to maximize the total intensity of the neutron beam while, ideally, minimizing undesired fast neutrons and γ-rays from the source. This can be achieved with neutron optics, using curvatures and neutron mirrors. The end-stations, also called experimental halls, may have various instruments and detector components. The total layout of a neutron beamline is usually several (from around 10 to over 100) meters long.

Due to the nuclear reactor nature of any neutron source, there is an enormous amount of heat that must be dissipated. The interest in continuous and intense

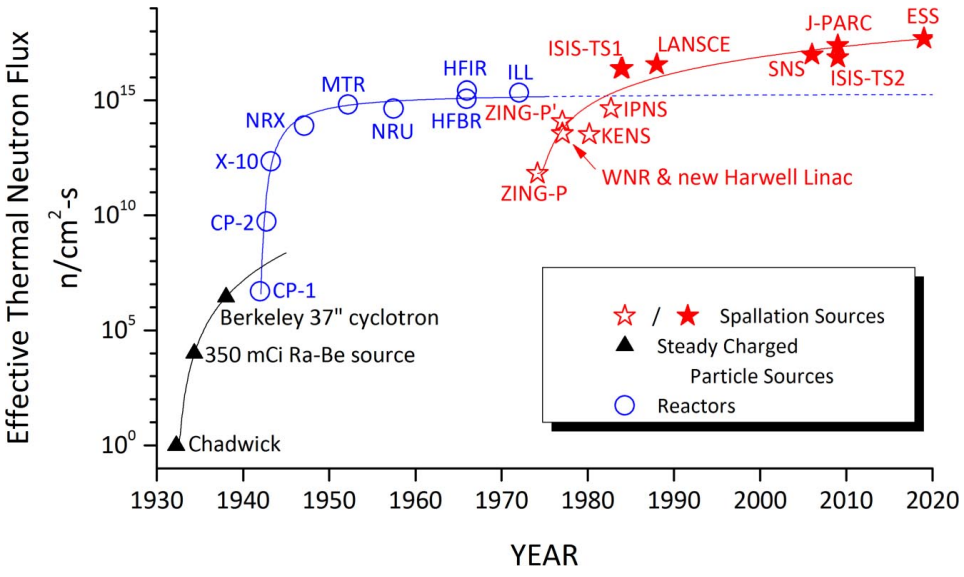

Figure 2.3.1: History of development of neutron sources. Extract from Guthrie [50].

neutron production means that heat transfer is a limiting factor when scaling up neutron production. Modern high-flux reactor sources reached a neutron flux plateau in recent years, as illustrated in Figure 2.3.1, due to intrinsic limits in heat dissipation. This led to an increased interest in constructing new and more intense spallation sources. Currently the most intense spallation source in the world is the American Spallation Neutron Source (SNS), located in Oak Ridge, Tennessee and part of the Oak Ridge National Laboratory (ORNL). A new spallation source in Europe, the European Spallation Source (ESS), is at its late stages of construction in Lund, Sweden. (The neutron flux suggested for ESS in Figure 2.3.1, the highest brilliance in the world, accounts for the initially planned 5MW design. The current design projects a 2MW operation to be upgraded in the near future.)

2.3.1 Neutron moderation

Neutrons have kinetic energy (or velocity) and because they are a result of a nuclear reaction neutrons are extremely energetic. Neutrons slow down when inelastically colliding with materials, particularly hydrogen-rich materials such as paraffin and water, in a process termed moderation. Often neutron sources are surrounded by H_2O tanks for moderation, and reactor sources rely on moderation at the core because slower neutrons are more prone to being captured by the core (necessary for a continued production). Eventually neutrons achieve thermal equilibrium with the moderator,

arriving at a Maxwellian distribution of velocities, i.e., a probability distribution of particle velocities in a system in thermal equilibrium. The distribution of velocities is determined by the temperature of the particles. In beamlines adapted to condensed matter research, neutrons are moderated to near room temperature with wavelengths comparable to inter-atomic distances, what is referred to as thermal neutrons.

2.3.2 Time-of-flight neutron count

The pulsed nature of spallation sources is not exclusive to accelerator-based sources, but the vast majority of reactor sources produce neutrons at a constant flux. Reactors can also produce a pulsed neutron beam by equipping mechanical choppers, devices designed to periodically interrupt the neutron beam for a well-defined duration. The advantage of a pulsed neutron beam travelling with a distribution of velocities is that their time-of-flight (TOF), i.e., the time it takes for each neutron to arrive from the end of the moderator to the detector, is a function of neutron velocity and, therefore, its wavelength (see Section 2.4). Pulsed neutron sources produce an intrinsically energy-dispersive beam, which is advantageous in scattering analyses.

2.4 Nuclear Scattering

Neutrons interact with matter through different mechanisms. If no interaction occurs neutrons are transmitted. Neutrons may be absorbed by materials usually leading to fission or atomic excitation. The most common type of interaction between neutrons and matter is scattering or deflection.

Neutron nuclear interactions are confined to the *strong force*, which acts over very short scales, ca. 10^{-15} m. The interaction probability is rather small, so thermal neutrons penetrate materials typically $\sim$1 cm before nuclear scattering occurs. The scattering intensity is thus orders of magnitude smaller than that of X-rays, and neutron scattering for research will require larger amounts of sample.

Due to the quantum-mechanical nature of particle dynamics, neutrons can also be represented as waves in what is called wave-particle duality. While neutrons possess attributes of a particle, e.g., momentum and kinetic energy, they can also have characteristics of a wave, e.g., wavelength and frequency. The momentum p, and wavelength λ and frequency ν of a wave-particle are correspondent via the de Broglie equation,

$$p = \frac{h}{\lambda}, \tag{2.4}$$

and the Planck-Einstein equation,

$$E = h\nu = \frac{hc}{\lambda} \tag{2.5}$$

where E is the kinetic energy, h is Planck's constant and c is the speed of light.

When neutrons are moderated to room temperature, their average kinetic energy given by $E \approx k_B T$ (where k_B is Boltzmann's constant and T is the moderator temperature) is of about 0.026 eV, which corresponds to a de Broglie wavelength of $\lambda \approx 1.8 \times 10^{-10}$ m.

Neutron properties make the neutron a very effective probe of condensed matter. Its zero charge means that it does not interact with electric fields. The magnetic moment of the neutron makes it also a probe of magnetism, because neutrons are scattered from unpaired electron spins and nuclear spins in materials.

2.4.1 The scattering process

Neutron scattering is a technique used to study the properties of materials, such as their structure and composition.

A simple scattering experiment can be schematized as shown in Figure 2.4.1. Incident neutrons represented as a wave vector $\mathbf{k}_\mathrm{i}$ are deflected to a final direction $\mathbf{k}_\mathrm{f}$. The scatterer nucleus is represented at the origin. The direction of $\mathbf{k}_\mathrm{f}$ is defined by the angles 2θ and ϕ.

2.4.2 Cross-section

Neutrons that interacted with the nucleus and scatter can be quantified by the total cross-section (σ_{tot}) defined by the number of neutrons scattered in all directions per second divided by the incident flux [47].

When measuring neutron scattering with a neutron detector of area dA, only neutrons scattered per second into a solid angle dΩ are counted. The differential cross-section captured by a detector also accounts for the detector count-rate and efficiency.

2.4.3 Scattering length

It is essential to quantify the interaction of neutrons with various isotopes or elements. The interaction between a neutron and a single atom can be then expressed simply by a single constant:

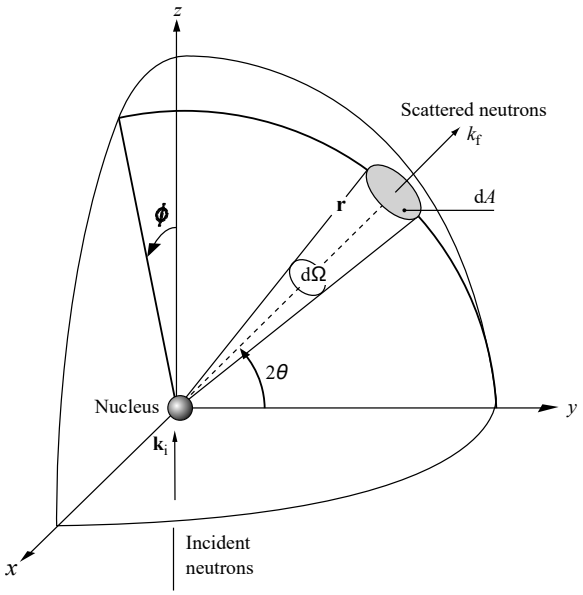

Figure 2.4.1: Schematic of a general neutron scattering experiment. Extract from Willis and Carlile [51].

$$\frac{\mathrm{d}\sigma}{\mathrm{d}\Omega} = |b|^2 \qquad and \qquad \sigma = 4\pi|b|^2 \tag{2.6}$$

b (in fm units) being defined as the neutron scattering length, a property of the scattering nucleus. b depends on the nature of the nucleus and is non-linearly sensitive to the atomic number (Z) and the mass (A). This creates a great contrast between neutron and X-ray scattering. One powerful consequence is a high sensitivity of the neutron beam to some light elements, notably hydrogen, and to the difference between atoms with similar atomic number or even isotopes.

In the absence of a complete theory of nuclear structure, scattering lengths cannot be calculated and must be measured experimentally. A list of scattering lengths with corresponding cross sections relevant to CHs in this work is given in table 2.1. Most relevant to neutron scattering is its significantly large sensitivity to hydrogen, particularly the incoherent cross section of ^{1}H. Other elements such as vanadium and aluminium produce near zero coherent and incoherent scattering, respectively, and are often used as transparent materials to neutrons (e.g., as sample containers). Unlike the atomic scattering factor of X-rays, b can be a negative number if there is a phase change between the incident and scattered beam. Appropriate molar ratios between

Table 2.1: Neutron scattering lengths and cross sections, adapted from Sears [52]

Isotope	**Abundance** [1]	b_{coh} [2]	b_{incoh} [3]	**Coh xs** [4]	**Incoh xs** [5]	**Tot xs** [6]	**Abs xs** [7]
H	—	-3.739	—	1.7568	80.26	82.02	0.3326
^{1}H	99.985	-3.7406	25.274	1.7583	80.27	82.03	0.3326
^{2}H	0.015	6.671	4.04	5.592	2.05	7.64	0.000519
^{3}H	*	4.792	-1.04	2.89	0.14	3.03	0
O	—	5.803	—	4.232	0.0008	4.232	0.00019
^{16}O	99.762	5.803	0	4.232	0	4.232	0.0001
^{17}O	0.038	5.78	0.18	4.2	0.004	4.2	0.236
^{18}O	0.2	5.84	0	4.29	0	4.29	0.00016
C	—	6.646	—	5.551	0.001	5.551	0.0035
N	—	9.36	—	11.01	0.5	11.51	1.9
Ne	—	4.566	—	2.62	0.008	2.628	0.039
Ar	—	1.909	—	0.458	0.225	0.683	0.675
^{36}Ar	0.337	24.9	0	77.9	0	77.9	5.2
Xe	—	4.92	3.04	2.96	0	—	23.9(1.2)
Al	100	3.449	0.256	1.495	0.0082	1.503	0.231
Ti	—	-3.438	—	1.485	2.87	4.35	6.09
V	—	-0.3824	—	0.0184	5.08	5.1	5.08
Zr	—	7.16	—	6.44	0.02	6.46	0.185

[1] Natural abundance (%). If not specified, the natural average is listed
[2] Bound – restricted by a chemical bond or a lattice – coherent scattering length (fm)
[3] Bound incoherent scattering length (fm)
[4] Bound coherent scattering cross section (barn)
[5] Bound incoherent scattering cross section (barn)
[6] Total bound scattering cross section (barn)
[7] Absorption cross section for 2200 m/s neutrons (barn)
* Not present in nature or no meaningful natural abundance be given

elements with negative and positive b may even produce alloys and ceramics with null scattering.

2.4.4 Elastic scattering

Because neutrons exchange momentum with the sample, the wave vector **k** changes direction. The momentum transferred to the sample is defined as the wave vector **Q**, which due to the law of momentum conservation, is given by

$$\mathbf{k}_i - \mathbf{k}_f = \mathbf{Q}. \tag{2.7}$$

Energy can also be exchanged with the sample, and the magnitude of **k** will then

change. Neutron scattering is thus given by the values of ($\mathbf{Q}$, E). The scattering is called "elastic" if there is no change in energy, $E = |\mathbf{k}_i| - |\mathbf{k}_f| = 0$ exactly and $|\mathbf{k}_i| = |\mathbf{k}_f| = 2\pi/\lambda$.

By equating the energy transfer to zero, we have the two-body collision problem with trigonometrical solution

$$\frac{|\mathbf{Q}|}{2} = |\mathbf{k}_i| \sin\theta = \frac{2\pi}{\lambda} \sin\theta \tag{2.8}$$

where 2θ is the angle between $\mathbf{k}_i$ and $\mathbf{k}_f$, as represented in Figure 2.4.1. For crystalline materials, a particularly strong elastic scattering occurs when $|\mathbf{Q}| = \mathrm{Q}$ is equal to a reciprocal lattice vector of the crystal:

$$\mathrm{Q} = \frac{2\pi}{d}, \tag{2.9}$$

where d is the spacing of the (h, k, l) set of crystal planes. Note that for disordered materials or powders, the structure factor is considered isotropic and only depends on the magnitude of $\mathbf{Q}$. Setting $\mathbf{k}_i = 2\pi/\lambda$, we arrive at the Bragg condition for diffraction:

$$\lambda = 2d \sin\theta. \tag{2.10}$$

Bragg diffraction

Considering incident waves arriving at a regular crystalline lattice with inter atomic distance d. For two scattered waves λ_1 and λ_2 to be in phase, λ_2 has to travel its extra trajectory an integer number of times its wavelength, $n\lambda$ ($n \in \mathbb{Z}$). The Bragg condition is therefore better described by the equation

$$n\lambda = 2d \sin\theta. \tag{2.11}$$

This relationship leads to two main approaches to collect diffraction data, (i) angle-dispersive instruments relying on the variation of the diffracted angle with a monochromatic (single wavelength) incident beam; and (ii) energy-dispersive instruments accounting for the differential diffracted beam energy at a given angle. The latter is commonly exploited in spallation neutron sources due to the nature of the moderated neutron pulses. The poly-chromatic neutron beam is then diffracted by the sample and the differential data with respect to energy dispersion is analyzed via TOF. The resulting diffraction pattern, whether energy-dispersive or angle-dispersive, is called a diffractogram.

Calculation of the whole pattern of a diffractogram is often possible. In the Rietveld method [53], scattering intensities can be calculated for any set of model crystal structures. The scattering profile accounts for background shape, peak positions and

intensities, and peak profile. Peak positions at angles/TOF are determined by the neutron wavelength, instrument geometry and lattice parameters. Intensities are calculated according to assumptions about peak profiles and how these vary across the pattern. Positional and thermal parameters of each individual atom in a phase also implicate intensity changes.

In a Rietveld refinement, parameters are varied so as to obtain the best possible fit between the calculated and the observed patterns. The method leads to good agreement between predicted and observed diffraction patterns, allowing tuning of phase parameters and insights about the crystal structure of the scattering analyte. Rietveld refinement allows crystal structure refinement in polycrystalline (powder) samples. It is routinely used in the characterization of crystalline materials to identify phase composition and impurities.

Disordered systems, including liquids and amorphous materials, do not produce sharp peaks due to the lack of a periodically repeating structure. Information on the relative atomic positions (short- and medium-range correlations between pairs of atoms) is contained in the structure factor as a function of momentum transfer.

2.4.5 Inelastic scattering

Inelastic neutron scattering (INS) is an ideal spectroscopy technique to observe the vibrational modes in ice and CH structures as well as that of enclathrated hydrogenous guests (e.g., CH_4, THF, H_2) as it is extremely sensitive to ^1H. As opposed to optical vibrational spectroscopies, e.g., infrared and Raman, INS is a nuclear process and the electronic contributions (dipole moment and polarizability) that make the intensities of infrared and Raman spectra so complex to calculate are absent. This also results in that all vibrational modes are allowed [54].

2.4.6 Coherent and incoherent scattering

The scattering process may give interference effects between scattered waves, yielding space and time relationships between different atoms. Collective excitation such as Bragg diffraction, phonons (mechanical oscillations in the crystal structure) and magnons (spin oscillations) produce coherent scattering. The interference in the so-called total scattering is called the coherent scattering cross section, σ_{coh}.

Incoherent scattering arises from the unequal distribution of scattering lengths in a sample, or atoms scattering unevenly. For instance, if the nucleus of a specific isotope has non-zero spin, each isotope has two different scattering lengths, b_+ and b_-, associated with whether the combined spins of the nucleus and the neutron are parallel or anti-parallel. Incoherent scattering does not produce interference and is seen as a "smeared" background underneath sharp signals in a diffractogram. Hydrogen (as

naturally abundant, 99.985% ^{1}H) scatters neutrons mainly incoherently due to the high σ_{incoh} of ^{1}H, and neutrons are particularly sensitive to hydrogen because of this interaction. Nevertheless, diffraction studies rely on coherent scattering that is obscured by the incoherent background, rendering ^{1}H disadvantageous for neutron diffraction (ND). ^{1}H can still be employed in diffraction studies in e.g., isotope substitution studies. In this case, the incoherent scattering background may be modelled or excluded. Diffraction studies of hydrogen-bearing materials are nevertheless a significant portion of the applications of neutrons, and this is done by employing the isotope ^{2}H (deuterium or D) which scatters dominantly coherently (cf. Table 2.1).

An additional advantage of ND is that neutrons diffracted are not modulated by a form factor the same way as, e.g., X-ray diffraction (XRD). The form factor is effectively a measurement of the size of the scatterer. In the case of probes e.g., X-rays, electrons, the scatterers are electron clouds. Because neutrons are scattered by the much smaller nuclei, neutron nuclear scattering is practically a point-like phenomenon. The form factor modulates the scattering profile with a Q dependence of the diffracted radiation. Data at higher Q are dampened by the form factor, which limits the d-spacings that can be achieved. As a consequence, neutron scattering may achieve greater spatial resolution. Neutrons scattered at higher Q are essential in studies of local structure, e.g., of glasses and amorphous materials.

Total Scattering and PDF Analysis

In a crystalline material, the nuclei are arranged in a regular array. Liquids and amorphous systems also have short- and medium-range order, but they lack the long-range periodicity found in crystals. Medium-range order is defined as beyond the nearest neighbor but no longer than the distance that produces diffraction lines characteristic of crystal structure [55]. The single differential scattering cross section of a group of atoms is modified by a structure factor:

$$\frac{\mathrm{d}\sigma}{\mathrm{d}\Omega} \propto \mathrm{S}(\mathbf{Q}), \tag{2.12}$$

where $\mathrm{S}(\mathbf{Q})$, the structure factor, depends on the positional correlation between particles.

The PDF method, introduced Chapter 1, is useful in the study of powdered samples, liquids, and amorphous materials. It's based on structure factors and the relationship between real-space (r) atomic pair density and total scattering intensity in Q space. The PDF is obtained by the Fourier transform of the $\mathrm{S(Q)}$. There are different notations to PDF and radial distribution functions (RDF) which emphasize particular features of the correlation functions. These functions usually relate to each other by scaling with r or the atomic number density in all directions.

3

Sample Environment

Sample environment methodologies allow the analysis of samples at conditions (e.g., temperature, pressure, electric or magnetic fields) other than normal conditions of temperature and pressure (NTP).

A great variety of sample environments is possible with *in situ* neutron scattering experiments. Because neutrons are electrically neutral, they readily penetrate most substances, including metals and construction materials. This allows that a sample can be held within bulky sample environments (e.g., cryostats, furnaces, reaction vessels and pressure cells) and still scatter neutrons efficiently.

This chapter describes sample environment apparatuses used for high-pressure, low-temperature neutron scattering experiments and underlying principles. The last section also describes the use of molecular simulations to reproduce materials in such conditions.

3.1 High Pressure

High pressure refers to a condition in which the force exerted is greater than the atmospheric pressure. Pressure is the force per unit area (by definition) and is typically measured in units of pascals (Pa), atmospheres (atm) or bars (metric equivalent of atmospheres, 1 bar $\approx$ 0.99 atm).

High pressure (HP) can be generated in a number of ways, such as compression (application of force) or by increasing the number of molecules or temperature of a gas.

To transmit pressure to a sample, a pressure-transmitting medium is used, such as anvils or solid/fluid media. If the medium is solid and has a flat interface, it will exert uni-axial pressure (compression along one axis). If the medium is fluid, it can exert pressure isotropically, referred to as hydrostatic or fluid static compression.

Pressure is a fundamental thermodynamic variable and HP can have various effects on matter. At high pressure, the electronic structures and atomic arrangements of a material can be altered. The effects of high pressure on a sample can be studied after decompression (*ex situ*), but *in situ* studies are necessary when changes are reversible or if the material undergoes additional changes upon release from high pressure.

Very high static pressures are only possible with small sample volumes. Neutron scattering in combination with HP is therefore disadvantageous and investigations are typically restricted to below 150 kbar.

3.2 Low Temperature

Low temperature can be produced in a laboratory in several ways but is usually accessed by inserting samples (or pressure cells) in a closed-cycle cryostat. Cryostats use liquefied gases such as liquid helium or LN_2 to cool samples thermally isolated from its surroundings by vacuum. Temperatures of 77 K (LN_2 cryostat) are routinely used. Temperature control is then achieved by electric (resistive) heaters and thermometers.

More generally, cooling can be achieved by various methods such as Peltier principle (thermoelectric cooling), compressors (adiabatic cooling), or submerging the sample in a cooling bath or flushing cooling liquid through its surroundings (convective cooling).

These cooling techniques can be combined with HP techniques. It is important to note that HP, LT research often requires specialized equipment and techniques. Cooling technologies may hinder HP, LT experiments by blocking ancillary equipment and obstructing the probe beam path. Concurrently, many materials ductile at room temperature become brittle at extremely low temperature. Embrittlement of materials such as metal components of pressure cells can lead to mechanical failures. HP, LT experiments require thus especially designed pressure cells with appropriate materials and geometries which will be described in the following sections.

3.3 Gas Pressure Cells

Gas pressure cells allow compression of samples with volumes of 1–10 cm^3 to pressures up to a few kbar. Characteristically, pressure is achieved by introducing gas, which acts as pressure transmitting medium, into the sample chamber. Pressure can be easily controlled

by gas injection/ejection and measured with standard pressure gauges attached to the inner volume of the cell. Gas cells can be store-bought or built with HP tubing and gas-tight fittings. Once loaded with gas, these cells can be safely handled, transported or stored in refrigerators for cooling. In this work, gas cells were used for the synthesis of most CHs. More details on the synthesis procedure are given in Chapter 4.

3.4 Piston Cylinder and Clamp Cells

The piston cylinder apparatus is widely used in HP and high temperature experiments, particularly in geological studies. A piston cylinder comprises of a compound construction of hollow cylinders and pistons. A piston is then hydraulically shifted to compress the sample within the inner cylindrical volume. A compressor refrigerator system can be adapted to piston cylinders, as displayed in Figure 3.4.1, for simultaneous HP, LT experiments.

In this work piston cylinder experiments were performed for the *in situ* measurements of thermal properties, thermal conductivity and heat capacity per unit volume. Thermal properties are characteristically unique in CHs and very distinct from those of ices [57], and are a routine tool used to identify glass transitions [58]. These properties were measured with the hot-wire method: a wire inserted in a medium (here, within the piston cylinder) is heated by a constant power. The temperature rise can be measured by the resistance of the wire and occurs in a time-dependent way. By solving the heat equation of the medium, i.e., the descriptor of the distribution of heat within the medium over time, thermal conductivity and heat capacity of the medium are determined [59].

A clamp cell is a kind of miniature piston cylinder pressure device. Pressure is generated by applying an external force with a press and then locking it mechanically (see Figure 3.4.2). Samples are loaded into a capsule and transferred to the outer cylinder while compressed by two pistons on each side. Sample volumes are similar to gas cells, but higher pressures, beyond 10 kbar (to up to a ca. 20 kbar limit [60]) can be reached. Clamp cells are compact and can be safely transported once loaded. Their disadvantage is that the cell is pressurized and locked outside the neutron instrument, and the pressure cannot be changed from the locked target pressure during an experiment.

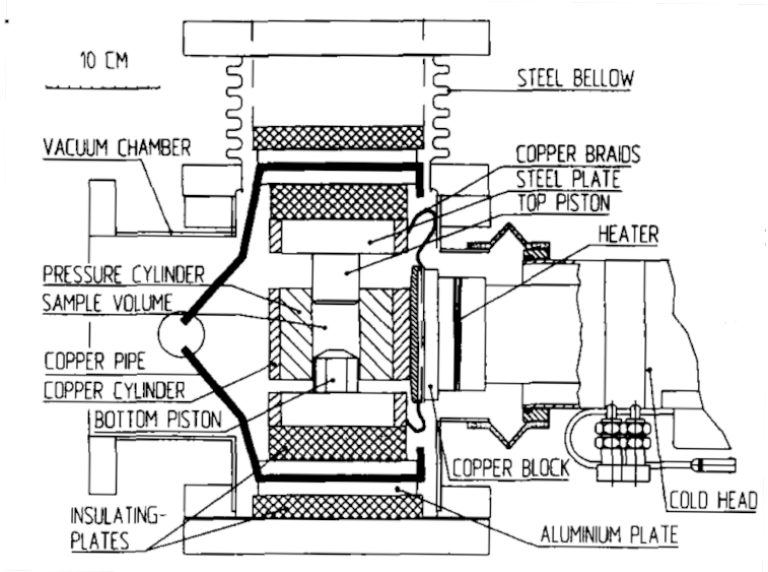

Figure 3.4.1: HP, LT piston cylinder apparatus. Figure adapted from Andersson and Inaba [56]. The apparatus described is present in the Physics Department of Umeå university in Sweden.

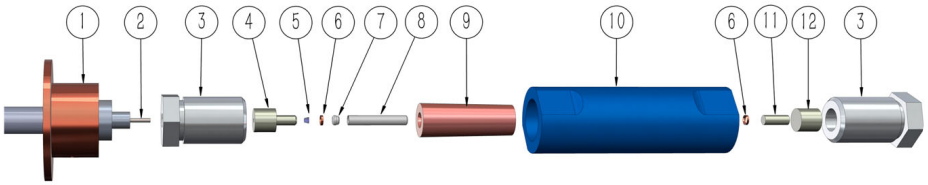

Figure 3.4.2: Schematic view and full assembly of a clamp cell. (1) Cryostat sample stick; (2) Optical fiber; (3) Locking nut (Al-alloy); (4,11) Pistons (WC). The left piston has a hole for an optical fiber and (5) a diamond anvil; (6) Anti-extrusion rings (Cu); (7,8) Sample container (Teflon); (9) Inner sleeve (CuBe or NiCrAl alloy); (10) Main body (Al-alloy); (12) Support spacers (WC). Extract from Podlesnyak et al. [60].

3.5 Paris-Edinburgh Press

The Paris-Edinburgh cell (PEC) is a crucial tool in HP neutron research. It allows the study of the effects of high pressure on materials by exposing them to controlled environments while simultaneously collecting neutron scattering data.

PECs are hydraulic presses that allow compression of samples with volumes of 10-100 mm^3 routinely up to 0.1 Mbar. They have been first developed in the early 1990s by the groups of Jean-Michel Besson (Pierre et Marie Curie University in Paris, France) and Richard Nelmes (The University of Edinburgh, UK). The PEC is designed for neutron scattering experiments with adequate apertures for the incident and scattered beams, but nowadays it has several applications beyond neutron scattering.

There are two types of load-frame designs: the original four-column V-design and the more recent two-column VX-design. The fewer columns in the VX design allow a wider beam aperture and enable diffraction at angles greater than 90°. This is particularly valuable in total scattering experiments because the high-Q scattering data range contains short-range atomic arrangement information, as discussed in Section 2.4.

Figure 3.5.1 shows a cross-section of the PEC types V and VX. To generate pressure, an oil pump injects oil to the bottom of the press where the piston is encompassed. As the piston chamber fills up with oil, the piston slowly raises in height. This movement generates huge forces on two opposing anvils which sandwich the sample tightly together. A close contact of the anvils is achieved by a threaded screw breech on the top piston. PEC load-frames allow tremendous tonnage capacity (maximum load in tons) while maintaining the overall press compact. The press usually weighs a few hundred kilograms and is portable.

PECs can be used in two distinct scattering geometries: transverse scattering, with the neutron beam passing through a rear aperture and scattering laterally (with an imposed diffraction angle near 90°) through the frame sides; and longitudinal scattering, with both incident and scattered beams crossing the cell laterally. Both geometries have advantages and disadvantages relating to background, angular aperture, beam attenuation and ancillary equipment.

The anvils and gaskets are the most important components of a PEC. Typically both have a curved profile with toroids (usually one or two) (cf. Figure 3.5.2). Toroidal anvils increase achievable pressures, while also allowing the sample gasket to remain gripped to the anvils which leads to a stable pressure distribution. Anvils are jacketed by steel rings and can be composed of various sintered hard materials (e.g., WC, diamond, boron nitride).

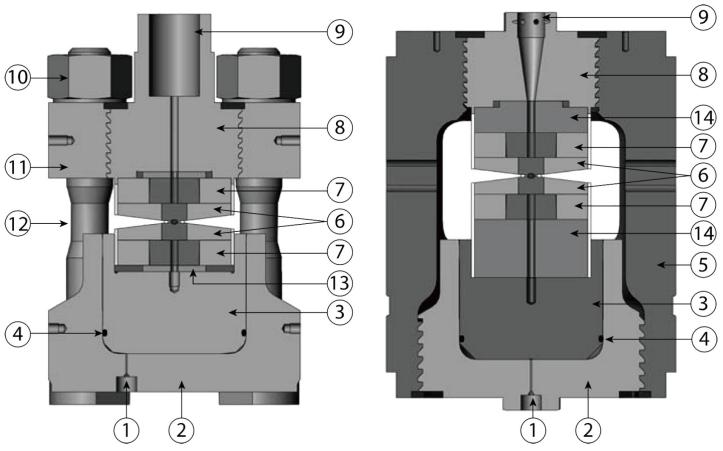

Figure 3.5.1: Cross section of Paris-Edinburgh press type V (left) and type VX (right). (1) Hydraulic fluid inlet; (2) cylinder; (3) piston; (4) O-ring seal; (5) load frame; (6) anvils; (7) backing plates (seats); (8) breech; (9) front collimator; (10) nut; (11) top platen; (12) tie rod; (13) backing disc; (14) steel spacer. Extract from Shi et al. [61].

PECs were the workhorse for all *in situ* neutron scattering experiments in this thesis. PECs are currently limited to diffraction experiments in neutron sources. Its capabilities allowed exploring *in situ* phase transformations and structural refinements of HP, LT phases. The following section describes the advent of HP neutron diffractometers with a design adapted for PECs. Subsequent sections then present the two dedicated HP neutron beamlines where experiments were run.

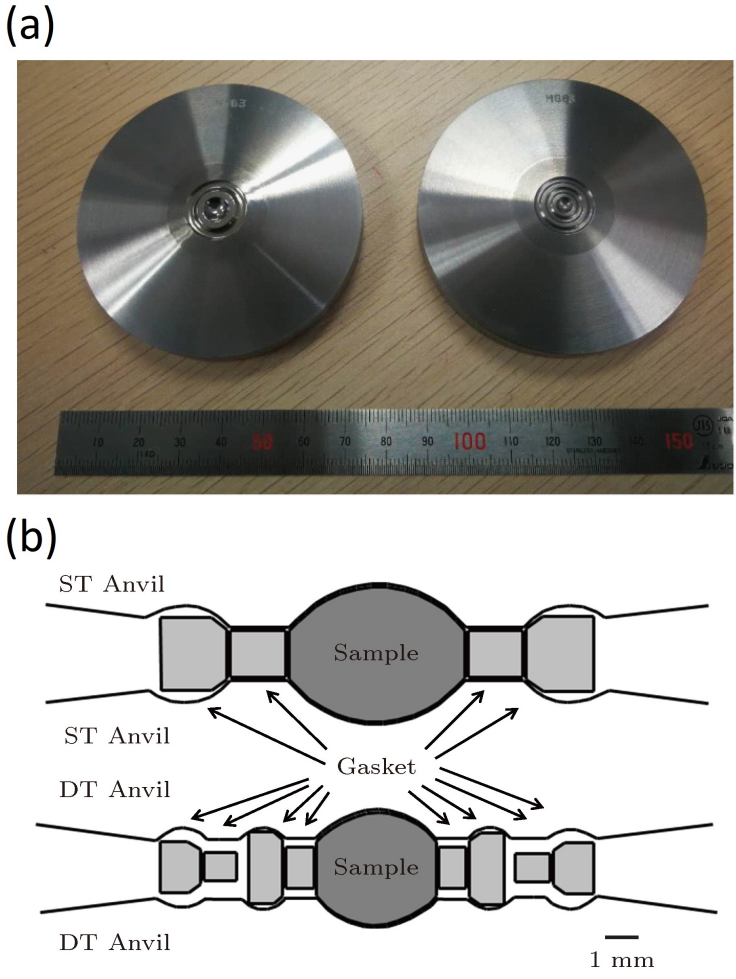

Figure 3.5.2: (a) The single toroidal anvil (left) and double toroidal anvil (right). (b) The single toroidal (top) and double toroidal (bottom) assemblies with anvil, gasket, and sample. Adapted from Shi et al. [61].

3.6 High-Pressure Neutron Diffraction

A conventional diffractometer measures total scattering cross-sections, including both Bragg and diffuse scattering, by utilizing an energy-resolved neutron beam and various components such as collimators to establish the direction of $\mathbf{k}_i$ and $\mathbf{k}_f$, and detectors to capture neutrons scattered at a particular angle. Energy resolution is attained through the use of either monochromators or TOF techniques.

The development of high-pressure neutron diffractometers was motivated by the advantages of using neutron scattering with high pressure. However, as discussed in Section 3.1, the necessarily large volumes of samples in neutron experiments hinder the maximum achievable pressure. The development of PECs thus enabled the creation of dedicated HP ND instruments.

A typical HP neutron diffractometer has thus three main components: a neutron guide or flight tube to focus the neutrons, a sample environment to surround the sample and control e.g., pressure and temperature, and neutron detectors (usually positioned at 90°).

3.6.1 PEARL

PEARL is the pioneer HP neutron diffractometer. Figure 3.6.1 illustrates PEARL's design. The (110 K) moderated neutron beam is collimated to a beam size of ca. 5 mm^2 at the sample position. The PEC can be positioned at 12.8 m from the end of the moderator, which results at a medium resolution ($\Delta d/d$ of ca. 0.64%) with high neutron flux. The press (typically a PEC) is contained within the sample tank in the figure, which can be evacuated or filled with LN_2.

When the PEC is mounted on the transverse geometry, the detector banks cover a range of ca. 80–100° diffracting angle (d-spacing range 0.5–4.1 Å). At the longitudinal geometry, the low-angle (ca. 20–60°) and high-angle (ca. 100–160°) banks can be accessed (d-spacing range 0.23–12.5 Å) at the expense of resolution. d-spacing ranges assume a standard TOF frame for the instrument [62]. TOF diffractometers use mechanical choppers, which are beam-stop devices adjusted to the neutron pulse frequency to eliminate frame overlap and define the observable Q-range by reducing the window of the wavelength spectrum allowed to reach the detector.

3.6.2 SNAP

SNAP is similarly a medium-resolution, high-flux diffractometer. The sample is positioned 15 m from the moderator and the neutron beam can be focused from 1 cm^2 down to 4 mm^2. It is equipped with moveable area detectors with an angular coverage

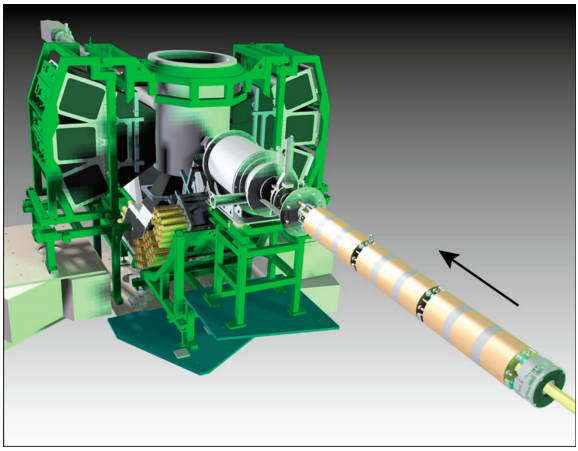

Figure 3.6.1: Schematic of the PEARL instrument. Extract from Bull et al. [62].

ca. 25–140°, which allow a d-spacing range of 0.4–9 Å.

Figure 3.6.2 shows a picture of the SNAP beamline, and Figure 3.6.3 shows the PEC mounted on the instrument.

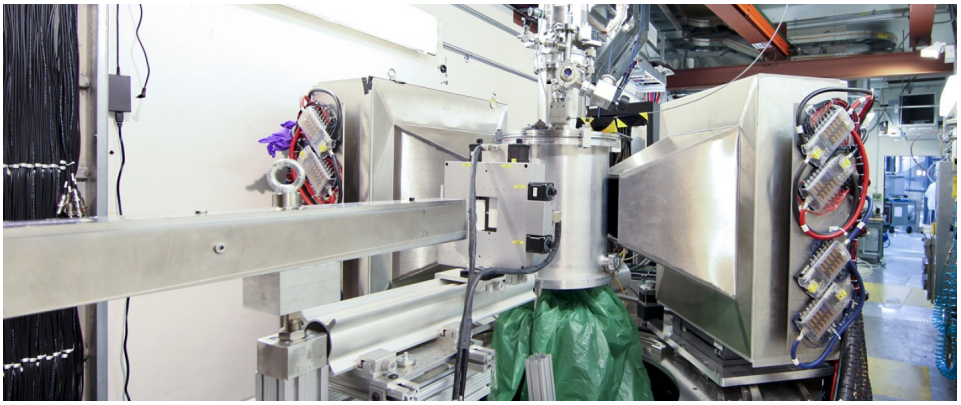

Figure 3.6.2: Picture of the SNAP beamline. Extract from https://neutrons.ornl.gov/snap, access 2023-01-12, permission under the Fair use Law.

Figure 3.6.3: Picture of a PEC mounted at SNAP in the longitudinal geometry.

3.7 Molecular Dynamics

Molecular dynamics (MD) is particularly capable in simulating samples at conditions which are challenging to access experimentally. MD helps resolve and interpret *in situ* experimental data. The method simulates the time-evolution of a collection of particles, usually atoms, by solving Newtonian equations of motion.

In this thesis, MD simulations were performed in two software packages, GROMACS [63] and LAMMPS [64]. Both packages are rubust open-source software that perform comparably. Of relevance to this work, these software employ different barostat algorithms (i.e., Nose–Hoover barostat is not available in GROMACS).

NPT (constant number of atoms, pressure and temperature) MD simulations of CH unit cells were reliably carried out with water force fields parametrized for ice [65]. Simulations were performed with periodic boundary conditions in all directions, but in simulations of disordered and amorphous systems large simulation boxes (ca. 30 Å wide) of multiple "unit cells" are necessary to avoid artifacts from periodicity. The crystalline ice lattice was generated using GenIce [66], a software that sets oxygen atoms at their crystallographic sites, randomizing the distribution of hydrogen atoms to account for the Bernal-Fowler ice rules, choosing a configuration of zero net polarization (cf. Section 1.2).

The results obtained from MD simulations were analyzed by examining the trajectories or snapshots of the atomic positions. Alternatively, the simulation data were used to generate $\mathrm{g}(r)$ and neutron $\mathrm{S(Q)}$ functions, which were then compared directly to experimental data. These methods of analysis allowed for a comprehensive interpretation of the experimental data and the behaviour and properties of the simulated CH systems.

4

Crystalline Clathrate Hydrates

This chapter will provide a comprehensive overview of the techniques and procedures involved in the preparation of crystalline CHs. Additionally, the chapter will describe an application of isotope substitution neutron scattering to solve the guest distribution within cages in Ar-CH (Paper I).

4.1 Synthesis

CHs crystallize from liquid water or ice when exposed to CH-forming guest species. The conditions and methods for preparing CHs will depend on the specific guest species and the type of CH being formed. Some CHs can be prepared at atmospheric pressure, while others require much higher pressures and lower temperatures to form. Although the mechanism of CH formation is still debated [67], synthesis is often rather straight forward.

CH synthesis differs mainly between CHs with guest gaseous species and species soluble in water. When guests are gases, CHs crystallize at the gas-ice interface under pressurized guest atmosphere. CHs with various gaseous guests can be synthesized with pressure vessels (e.g., gas cells) capable of producing and maintaining the formation conditions. With guests miscible in water, however, a guest solution at sufficient concentration can freeze directly as CH at atmospheric pressure.

The following sections give details about the synthesis of the CHs used in this work.

4.1.1 THF- and other water-rich CHs

THF and other ether or ketone compounds (like acetone, cyclobutanone, 1,3-dioxolane) are well miscible with liquid water, with solubilities $\geq$ 100 mg/mL at NTP. CHs with such organic molecules as guests are thus prepared with a long-established procedure [58] from a solution with the target stoichiometry mixed while cold and quickly brought below the freezing point (ca. 0–4 °C) at atmospheric pressure.

The synthesis proceeds by slow crystallization of the solution. The CHs crystallize with the CS-II with a stoichiometric composition 1 guest $\cdot$ 17 H_2O. Excess water in solutions crystallize as ice I_h and ice is a common contaminant in CH samples. The procedure leads to the full conversion of the water:guest solution into pure clathrate if the appropriate concentration is produced.

4.1.2 Ar- and Xe-CHs

Ng-CHs are synthesized in a gas pressure cell under pressurized Ng atmosphere below freezing temperature. Ar, Kr, Xe, and Rn require mild pressures (a few hundred bars) [16]. Ne requires kbar pressure to crystallize with the CS-II and Ne-CH preparation is described in the following section regarding CHs with low-Z guests. Figure 4.1.1 shows formation/dissociation boundaries for various gas CHs in this work.

As mentioned, ice $I_h \rightarrow$ CH conversion occurs at the ice grains surface and a thin CH layer forms rapidly over the ice surface, as observed experimentally [71, 72]. The continued conversion of ice grain cores requires transport of the gas species through the intervening CH layer. The growth of CHs is then a diffusion-limited process [73].

Accounting for this, a dedicated gas hydrate synthesis apparatus was put in place at the SNAP beamline. Figure 4.1.2 shows a picture of the apparatus. The idea was to freshen the ice grain surface and accelerate the CH synthesis. A HP stainless-steel Parr®(250 mL) vessel adapted to a tumbler allowed the use of ball bearings during CH formation. The entire apparatus was adapted inside a large freezer, so the pressurized vessel could be kept below freezing temperature while tumbled. This setup provides grinding to ice grains during CH formation, thus refreshing the ice surface for complete conversion.

^{36}Ar-CH, used in isotope substitution neutron scattering experiments, was prepared in much smaller (ca. 5 mL) pressure cells due to the expense of the gas. Xe-CH was also prepared in small pressure cells. 5 mL gas cells were built using Swagelok® pressure tubing and fittings. The small volume is adequate to prepare ca. 1 g of sample. The powdered ice precursor had to be finely ground and sieved to guarantee complete conversion and reduce reaction time. In this work, grain sizes smaller than 96 μm were used. When using expensive gases, original cylinders are often only slightly pressurized.

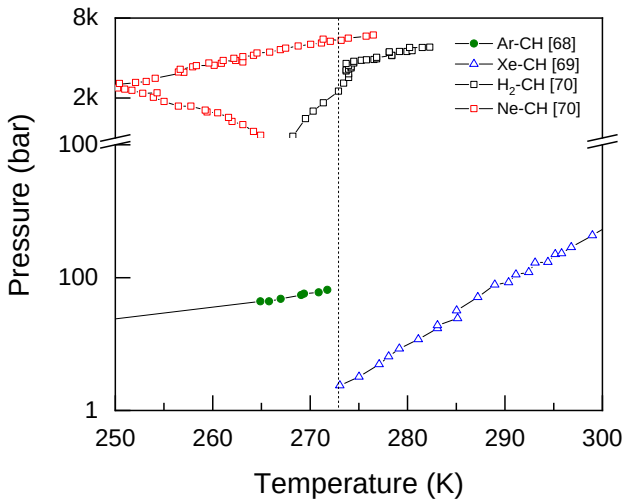

Figure 4.1.1: Experimental dissociation conditions (ice-hydrate equilibrium) of various gas CHs in this work. The dashed line marks 0 °C. Experimental data extracted from Mohammadi and Richon [68], Ohgaki et al. [69] and Dyadin et al. [70].

To build up pressures to the necessary hundreds bar, the original cylinders were connected to the gas cell and the noble gases condensed into it at LN_2 temperature. A pressure gauge and a release valve were used to secure and control the pressure. Figure 4.1.3 sketches the 5 mL gas cell design.

4.1.3 H_2- and Ne-CHs

The synthesis of CS-II H_2- and Ne-CH was undertaken similarly to other gas CHs, but the smaller-sized gases require much higher pressures, ca. 2 to 3 kbar [74] (cf. Figure 4.1.1).

To prepare CS-II H_2-CH, a HP rated vessel compatible for H_2 gas was filled with finely ground ice and loaded with pressurized gas with the use of a gas-pressure intensifier. The gas transfer was done with the sample vessel submerged in an eutectic ethanol-water bath slightly above freezing (ca. 155 K). The vessel pressurized with H_2 was then kept at 253 K for one week in an explosion-proof freezer (ordinary freezers may produce sparks). Ne-CH was prepared under similar conditions with the same apparatuses. Both syntheses produced virtually pure CS-II samples.

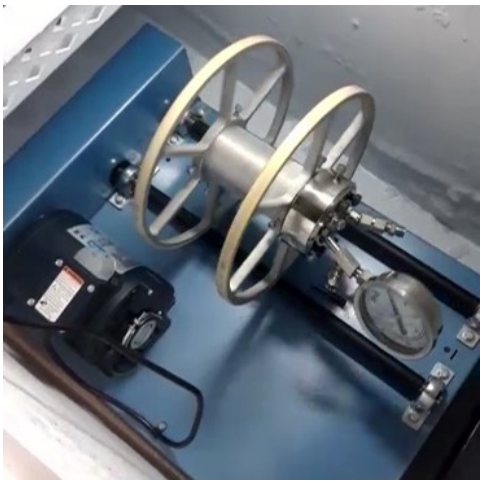

Figure 4.1.2: Gas hydrate synthesis apparatus constructed at the SNAP beamline, SNS. A Parr vessel adapted to aluminium wheels tumbles inside a closed freezer.

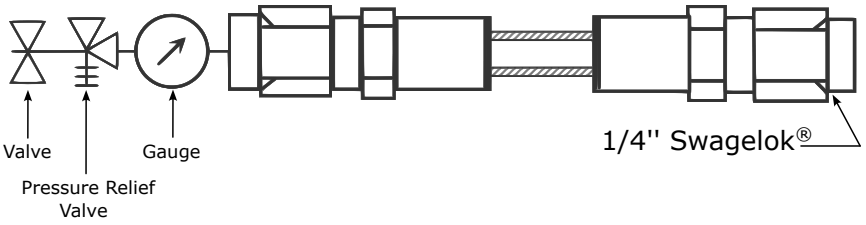

Figure 4.1.3: Gas cell built with Swagelok® pressure tubing and fittings.

4.2 Guest Disorder in CS-II Ar-CH

Clathrate formation conditions depend on the size and properties of the guest species, which affect the type of clathrate structure that forms, as discussed in Section 1.2. The stabilizing effect of the guests in CH structures is well described assuming only weak interactions [21]. The distribution of atoms within the cages probes details of guest-host interactions, as it indicates preferential coordination which in turn should be mirrored by the potential energy surface within the clathrate cage. Guest distribution in CH structures is influenced by factors such as the size and shape of the guests and cages, as well as pressure and temperature.

Ng-CHs are good model systems due to their spherical shape and chemical inertness. In the case of Ng-water interactions, Lennard-Jones potentials can be use to model the guest distribution within cages, as described by Davidson [21]. Figure 4.2.1 demonstrates this relationship with potentials calculated for Ng atoms within D cages (present in both cubic structures). Negative potential energies represent a stabilizing interaction.

Ar atoms are rather small (ca. 3.7 Å in diameter) with respect to the free diameter of H cages (6.6 Å, cf. Table 1.2). As a consequence, Ar in H cages should not be located at the center but distributed over off-centered positions. The guest position in CS-II Ar-CH has been studied using X-ray and neutron scattering and various modelling techniques [27, 29, 76, 77, 78, 79, 80, 81, 82], but the results are conflicting and incomplete.

One generally accepted structure for CS-II Ar-CH is the one reported by Manakov et al. [27]. These authors found that D and H cages are occupied by 1 and 1.8 Ar atoms, respectively. Multiple occupancy is, however, predicted to destabilize the ice framework and significantly increase the energy of the system [80]. Chazallon et al. [82] could not observe experimentally (using neutron spectroscopy) the characteristic vibrations predicted for doubly occupied CS-II Ar-CH. It is therefore assumed that CS-II Ar-CH at atmospheric pressure has either empty or singly occupied D and H cages.

More recently, the guest position in CS-II Ar-CH was studied at atmospheric pressure and low temperature by XRD. Yang et al. [79] described Ar disorder by a tetrahedrally two-site split position within H cages. In this model, D and H cages have much lower occupancies, 0.85 and 0.88 respectively. However, Ar scattering dominates the XRD pattern, and ND should be a better tool as deuterium scatters neutrons as efficiently as oxygen.

The difficulty of crystallographically assigning site occupancies for Ar atoms with neutron scattering lies in the small neutron scattering cross section of natural Ar (cf.

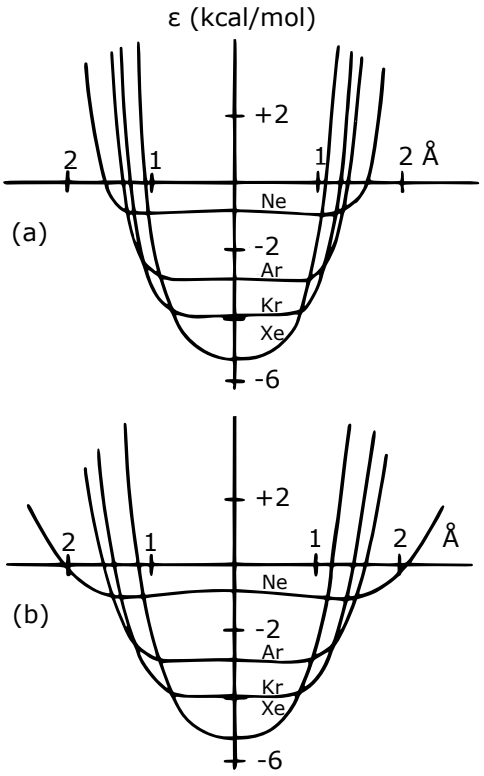

Figure 4.2.1: Lennard-Jones potential energy of Ng atoms modelled with London dispersion forces as a function of displacement from the center of D cages. Representations along (a) an axis joining the centers of two opposite water molecules, and (b) along two centers of pentagonal rings. Adapted from Barrer and Edge [75].

Table 2.1). Ar contribution represents only a small percentage of the information in ND patterns. In Paper I, we explore the possibility of enhancing the Ar guest structure information by means of isotope substitution ND. The coherent scattering length of ^{36}Ar is ca. 13 times larger than that of natural Ar. Isotope substitution is well established for PDF studies in non-crystalline systems such as glasses, but it has also been proven an effective method for the investigation of (problematic) crystalline materials, provided that suitable isotopes are available. Results present the solution of the guest disorder inside D and H cages in CS-II Ar-CH which turns out distinct from the aforementioned models.

ND patterns of fully deuterated, isotope substituted (Ar/^{36}Ar) Ar-CH were used to

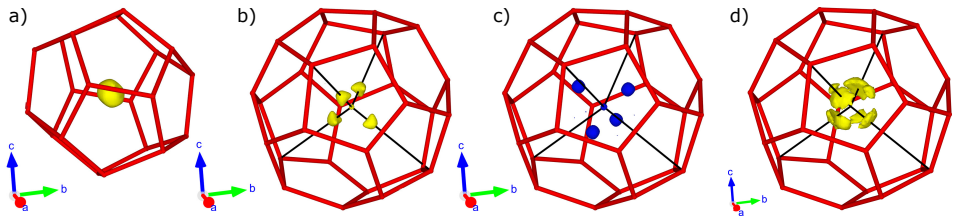

Figure 4.2.2: Difference Fourier maps of ^{36}Ar-CH at 20 K inside (a) D and (b) H cages in the CS-II unit cell. (c) Repeated Fourier map inside H cages after insertion of Ar atoms in the positions shown in (b). (d) MD simulated Ar atom free energy isosurface of 0.2 kJ/mol inside an H cage. Adapted from Paper I.

produce a difference Fourier map calculated between an empty CS-II model and the ND profile. The resulting diffraction intensities were plotted within the CH unit cell. Intensities indicated the distribution of nuclear densities from Ar atoms in cages, as shown in Figure 4.2.2.

Ar guests inside D cages occupy the cage center (Figure 4.2.2(a)). In the case of H cages, Ar atoms assume a disordered tetrahedron-like distribution with atoms facing oxygen atoms (Figure 4.2.2(b)). After including Ar atoms in these positions (with unconstrained occupancies), a second Fourier map revealed again a tetrahedron-like distribution with atoms now facing the centers of hexagonal faces (Figure 4.2.2(c)). The two tetrahedra are offcentered by a very similar value. The overall sum of both tetrahedra resembles a cuboid-like distribution. This two-step difference Fourier map led to a disordered model with best results in Rietveld refinements.

In MD simulated CS-II Ar-CH, the energy grid map inside H cages showed potential wells with a similar disorder, shown in Figure 4.2.2(d). MD estimated energy barriers between minima are ca. 0.25 kJ/mol, which strongly suggests that the disorder within H cages is dynamic.

Cage occupancies were determined with this model by Rietveld refinement with good reliability factors ($R_{wp} = 2.71\%$, $\chi^2 = 8.60$). The resulting occupancy of D cages was 0.894(7). The two positions within H cages were refined to 0.158(9) and 0.049(12) occupancy, equivalent to ca. 83% filled cages.

Lastly the temperature dependence of the lattice parameter/unit cell volume of Ar-CH was analyzed. ND patterns were collected for Ar-CH samples in the temperature range 20 to 95 K. Lattice constants and thermal expansions are comparable to Ne-, O_2- and N_2-CH, as shown in Figure 4.2.3.

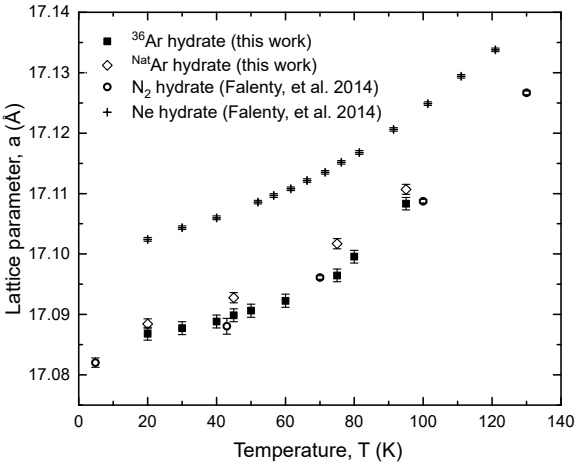

Figure 4.2.3: Lattice parameter versus temperature for ^{36}Ar- and ^{Nat}Ar-CH (squares and diamonds, respectively), in comparison to N_2- (circles) and Ne-CH (crosses). Extract from Paper I.

The diatomic gases are comparable in size to Ar and lattice constants are very similar. Guest-host interactions can be assumed to be very similar. The larger lattice parameter of CS-II Ne-CH can be attributed to the more attractive Ar-host interaction. This also impacts the occupancy of Ne atoms within cages. Ne-CH has D cages occupied at 86%, which is similar to Ar-CH. However, H cages are partially doubly occupied which is not possible in Ar-CH at atmospheric pressure.

The similarities in the temperature behaviour suggest that guest-host interactions in CHs are very similar. The nature of the guest does not significantly affect the thermal expansivity of the CS-II CHs. The following chapters will show that pressure will lead to significant differences between various CHs and their structures and phase behaviour.

5

Pressure-Induced Amorphization of Clathrate Hydrates

Applying external pressure to CS-I and CS-II type CHs at near room temperature leads to consecutive phase transitions into denser CHs and FIS, as discussed in Section 1.3. It is clear that the phase behaviour of CHs strongly depends on the nature of the guest, original clathrate structure (i.e., CS-I and CS-II) and composition. On the other hand, the high pressure behaviour of CHs at low temperatures has been rarely investigated. Examples of CHs displaying PIA are limited and the influence of the guest on their pressure-behaviour is still understudied.

This chapter discusses the PIA of CHs to CH-HDA and the non-recoverability of CH-HDA by summarizing results for CHs with large organic molecules (papers II and III) and Ngs as guests (Paper IV). This chapter also addresses the HP, LT behaviour of CHs with the low-Z species H_2 and Ne as guests, for which crystal-crystal transitions are observed (paper V).

5.1 Background

PIA of CHs was first observed with CS-II systems. Ross and Andersson [83] showed that THF-CH transformed at 1.1 GPa on isothermal compression at 130 K into a

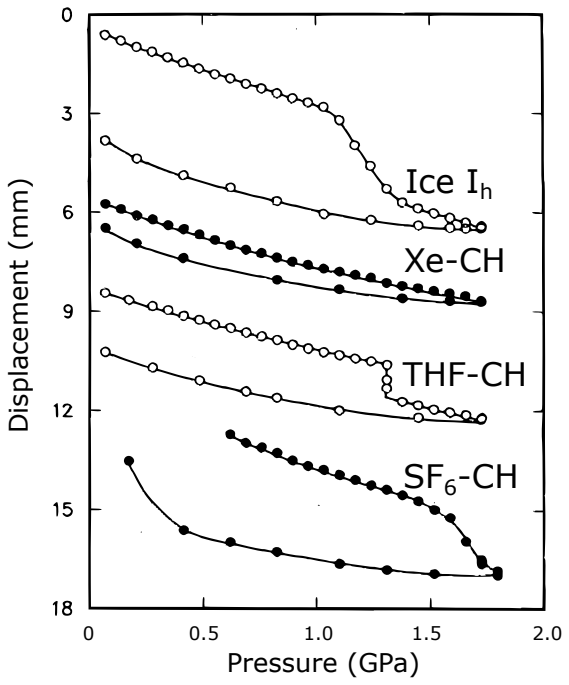

Figure 5.1.1: Piston displacement versus pressure for experimental isothermal compression at 77 K of various CHs. Adapted from Handa et al. [84].

densified state that was assumed to be amorphous. Later, Handa et al. [84] detected with piston cylinder experiments volume changes in CHs similar to those of ice I_h. In these experiments, shown in Figure 5.1.1, THF-CH and SF_6-CH showed PIA at 1.3–1.6 GPa at 77 K. Handa et al. [84] also investigated the CS-I Xe-CH, which did not amorphize at pressures up to 1.7 GPa. The authors suggested that the larger guest might have impacted the pressure of amorphization towards higher pressures. The two CS-II systems investigated by Handa et al. [84] share the same water-rich composition, 1:17. Andersson and Häussermann [58] showed that other CS-II CHs with large guests (1,3-dioxolane and cyclobutanone) followed a similar PIA behaviour.

CS-I has been less investigated in HP, LT experiments. Tulk et al. [85] showed CH_4-CH (same structure as Xe-CH) to undergo PIA at 3.2 GPa, 90 K.

An important distinction between water-ice HDA and CH-HDA is that decompression leads to the recrystallization of CHs even at low temperature. Handa

et al. [84] proposed that amorphized CHs generally cannot be recovered to atmospheric pressure because guest species will act as centers of nucleation, whereas Bauer et al. [86] suggested that the presence of crystalline remnants in CH-HDA may be responsible for the "spring-back" behaviour. Strässle et al. [87] connected the PIA of CHs (to CH-HDA) to a purely mechanical melting (based on a phonon instability), whereas ice showed a crossover from mechanical to thermal melting (governed by the free energies of the crystalline and amorphous states), the thermodynamic stability of CH-HDA being thus reversible on decompression. As will be discussed in the next chapter, Chapter 6, it is actually possible to recover amorphous CHs at atmospheric pressure. However, this requires that CH-HDA is first transformed into a different amorphous form (CH-VHDA).

5.2 PIA of Water-Rich CHs

Four different (CS-II) 1:17 CHs with guests THF, 1,3-dioxolane, cyclobutanone, and acetone were studied by thermal analysis (Paper II). All samples were pressurized to 1.3 GPa at ca. 130 K upon which they became amorphous at ca. 1.1 GPa.

The similar behaviour of the CHs is summarized in Figure 5.2.1 (acetone is excluded). As mentioned in the introduction, the thermal conductivity (κ) of crystalline CHs is exceptionally low (lower than 0.5 W/mK). The initial weak increase on compression up to ca. 0.8 GPa is the normal behaviour of κ with increasing density. On further compression, κ decreases, leading to a local minimum at 0.9–1 GPa, after which a sigmoid-shaped rise occurs. The decrease and minimum of κ has been interpreted with a disordered "precursor" state before PIA. The steep rise of κ at 1–1.1 GPa is then a consequence of PIA. For these CHs the densification upon PIA is about 20% (Paper II) and the associated increase in κ outweighs by far the otherwise expected decrease when becoming a completely disordered amorphous material.

It is noteworthy that the PIA behaviour of the water-rich 1:17 CHs appears to be quite independent on the kind of organic guest species. Further, there seem to be no, or very little, isotope effects.

THF-CH (fully deuterated) was investigated with ND on isothermal compression at 130 K up to 1.2 GPa (Paper III). Experiments were run on the PEARL instrument at ISIS, UK. Figure 5.2.2 shows neutron diffractograms. PIA was identified in ND experiments by the disappearance of diffraction peaks.

The relationship between lattice parameters and pressure was used to calculate the equation of state (EoS) of THF-CH at 130 K with the simple Murnagham relation

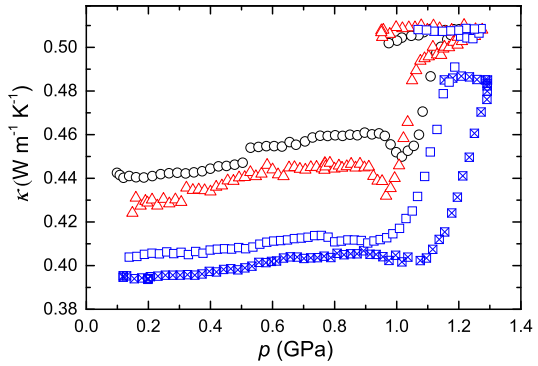

Figure 5.2.1: Heat capacity per unit volume on isothermal pressurization at 130 K of 1,3-dioxolane (triangles), THF (circles), and cyclobutanone (at 130 K, squares, and 117 K, crossed squares). Extract from Paper II.

$V_0/V = [p(B'/B) + 1]^{1/B'}$, where V is the volume at pressure p and V_0 is the volume at atmospheric pressure. The obtained bulk modulus (B) up to 0.7 GPa for THF-CH was 8.6(3) GPa, with its first derivative with respect to pressure (B') fixed at 4.0. The value appears significantly lower than that of hexagonal ice I_h (9.8(5) GPa [87], up to 0.5 GPa). The overall greater compressibility of THF-CH was thus linked to the greater empty volumes within D cages which accommodate a greater distortion on compression.

The main conclusion obtained from ND is that no intermediate phase can be detected before and during PIA. MD simulations however revealed that prior amorphization the hexagonal rings of H cages become severely deformed whereas the integrity of the empty D cages is maintained. This state probably coincides with the "dip" phenomenon in κ. The collapse of D cages is nevertheless responsible for the major density increase.

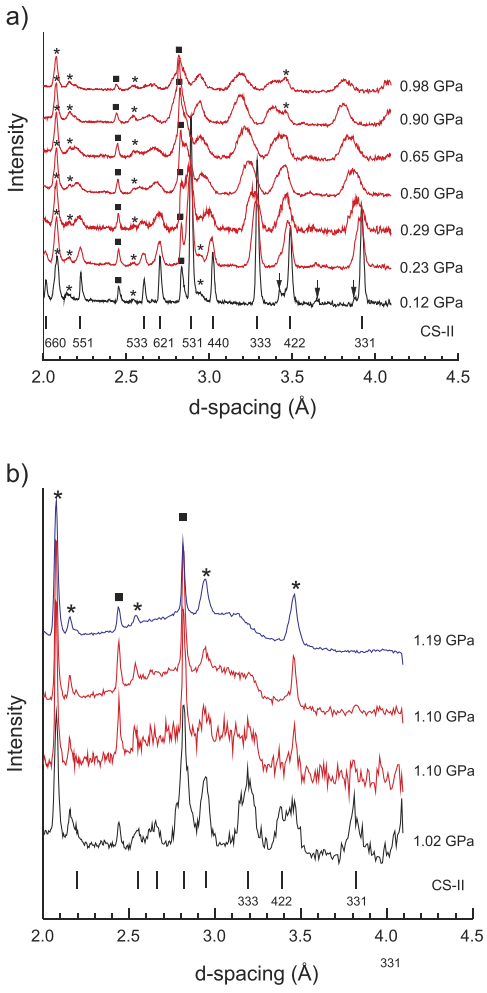

Figure 5.2.2: (a) ND patterns of THF-CH upon compression to ca. 1 GPa at 130 K. (b) Diffraction patterns with progressing amorphization on further compression. Pronounced anvil peaks are marked with asterisks, peaks from the pressure marker Pb are marked with solid squares, and peaks from ice I_h (contaminant) are indicated by arrows. Adapted from Paper III.

5.3 PIA of Ng-CHs

In Paper IV, ND experiments were performed to study the behavior of Ng-CHs at 95 K and at increasing pressures. The systems investigated in experiments were CS-II Ar-CH and CS-I Xe-CH. MD simulations were performed on Ngs Ne through Xe, each guest in either CS-I or CS-II. Results allowed the systematic investigation of the effect of guest size, cage filling and cage occupancy on the PIA phenomenon of CHs.

The experiments and simulations involved isothermally compressing the samples at 95 K until they reached a state of structural change. All Ng-CH systems were found to amorphize with pressure, regardless of the CH structure. However, the size of the guest and the hosting cage structure were found to influence the pressure of amorphization. Moreover, large guests such as Xe were found in both simulations and experiments to amorphize in a sluggish manner producing a semi-crystalline state before complete amorphization.

ND experiments were run at the SNAP instrument at the SNS. Compressions were carried out to up to 8 GPa for Xe-CH and up to 3 GPa for Ar-CH. Figure 5.3.1 shows *in situ* neutron diffractograms of both materials. The amorphization pressure for Ar-CH was found to be 1.4 GPa, which is similar to 1:17 CS-II CHs, but at a slightly higher pressure than the pressure of the ice I_h to HDA transition. On the other hand, the amorphization pressure for Xe-CH was observed to be 4.0 GPa, which is considerably higher than the amorphization pressure of CS-II CHs and similar to that of CS-I CH_4-CH. Like the amorphized water-rich CHs, both Ng-CH-HDA recrystallized on decompression.

The situation of CS-II Ar-CH is rather different than water-rich (1:17) CHs. Ar-CH composition, obtained by Rietveld refinement of ND data using the model described in Chapter 4, is $Ar \cdot 6.5\,H_2O$. Ar-CH PIA is, however, rather similar. This was also confirmed from MD simulations showing again severe deformation of the hexagon rings of H cages preceding overall collapse.

Xe-CH represented instead a special case in both experiments and MD simulations. The crystalline CS-I Xe-CH formed a unique semi-crystalline state prior to amorphization. In this state, Xe guests appeared to retain some degree of long-range ordering, observed experimentally producing diffraction peaks, while the water network appeared already amorphous. Figure 5.3.2 shows simulated and experimental diffraction patterns of Xe-CH at this state. Further compression finally led the material to complete amorphization. Figure 5.3.3 shows a snapshot from MD simulated CS-I Xe-CH as compared to CS-II Ar-CH throughout amorphization.

Experimental diffraction patterns on compression show the evolution of the CH

lattice volume, which was again used to produce the EoS relationship. For Xe-CH between 0 and 4 GPa the bulk modulus obtained was 12.7(3) GPa, while Ar-CH between 0 and 1.4 GPa appeared more compressible with bulk modulus 11.2(7) GPa.

The PIA of Ng-CHs was then systematically studied by MD simulations considering Ng = Ne–Xe, both types of structures, CS-I and CS-II, and various scenarios of cage fillings (i.e. both types of cages occupied or only one type and the other empty). Figure 5.3.4 summarizes the results presenting density changes with pressure in each system.

The systems investigated comprise of CS-I and CS-II CHs filled with each Ng with either occupied D or T/H cages (Figures 5.3.4(a-b)) or both types occupied (Figures 5.3.4(c-d)). Without a guest species ("empty" clathrate), both cubic clathrate structures amorphized at 1.2 GPa, which is very similar to hexagonal ice. Filling of large-sized H cages did not provide stability towards amorphization for CS-II, whereas filled small-sized dodecahedral D cages shifted PIA to successively higher pressures with increasing size of the Ng guest. For CS-I, filling of both kinds of cages, larger T and smaller D cages, acted to stabilize in a cooperative fashion. When fully occupied (referring to compositions $Ng \cdot 5.75\,H_2O$ and $Ng \cdot 5.67\,H_2O$ for CS-I and CS-II, respectively), both cubic structures exhibited a similar behaviour with PIA occurring in the pressure range of 1.3–2 GPa, depending on the size of the Ng.

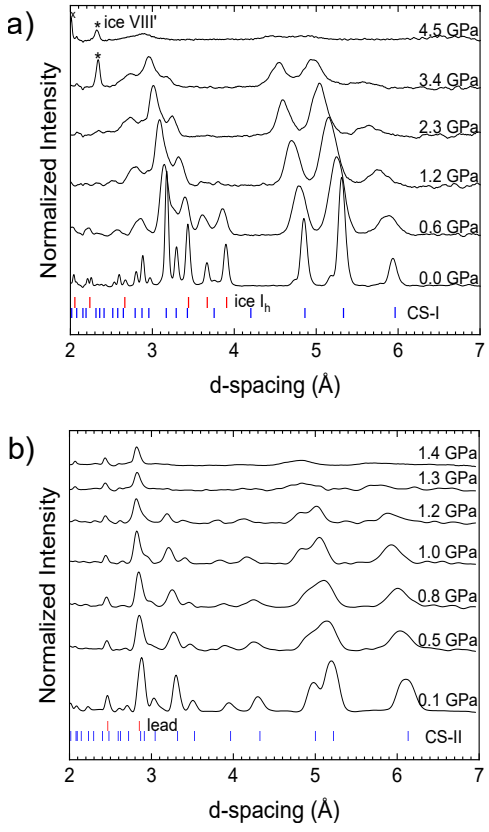

Figure 5.3.1: Evolution of the ND profiles of (a) CS-I Xe-CH and (b) CS-II Ar-CH upon compression. Tick marks show Bragg positions of allowed reflections for the fitted phases. Stars mark peaks from ice (111 reflection of ice VII or 112 reflection of ice VIII), which can be seen in (a) after recrystallization of HDA-ice above 2.5 GPa. Cross marks the 110 peak of iron as the steel anvil shades part of the beam at high pressures. Extract from Paper IV.

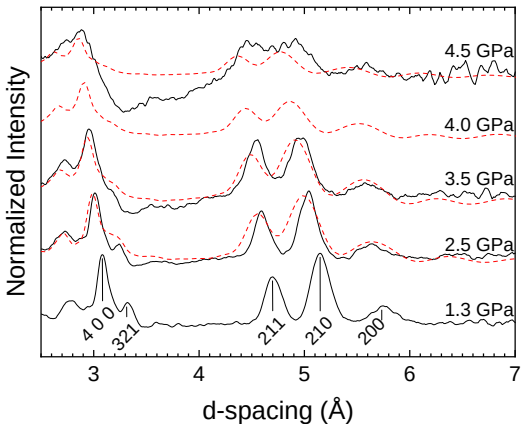

Figure 5.3.2: ND patterns showing the structural progression of CS-I Xe-CH with pressure in experiments and MD snapshots. Black lines represent experimental data. Red-dotted lines represent simulated patterns from MD snapshots. Patterns show no sudden change in the long-range structure, and the final pattern with still crystalline features is in good agreement with experimental data. Extract from Paper IV.

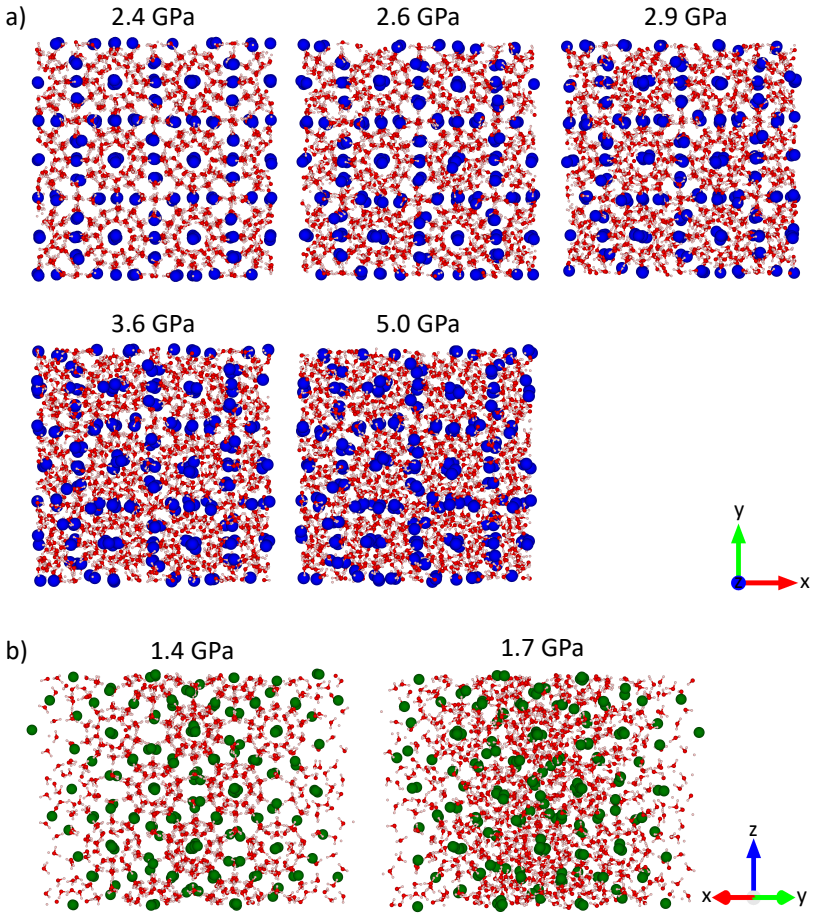

Figure 5.3.3: Structure section from MD snaphots comparing (a) Xe-CH and (b) Ar-CH at different pressures. Extract from Paper IV.

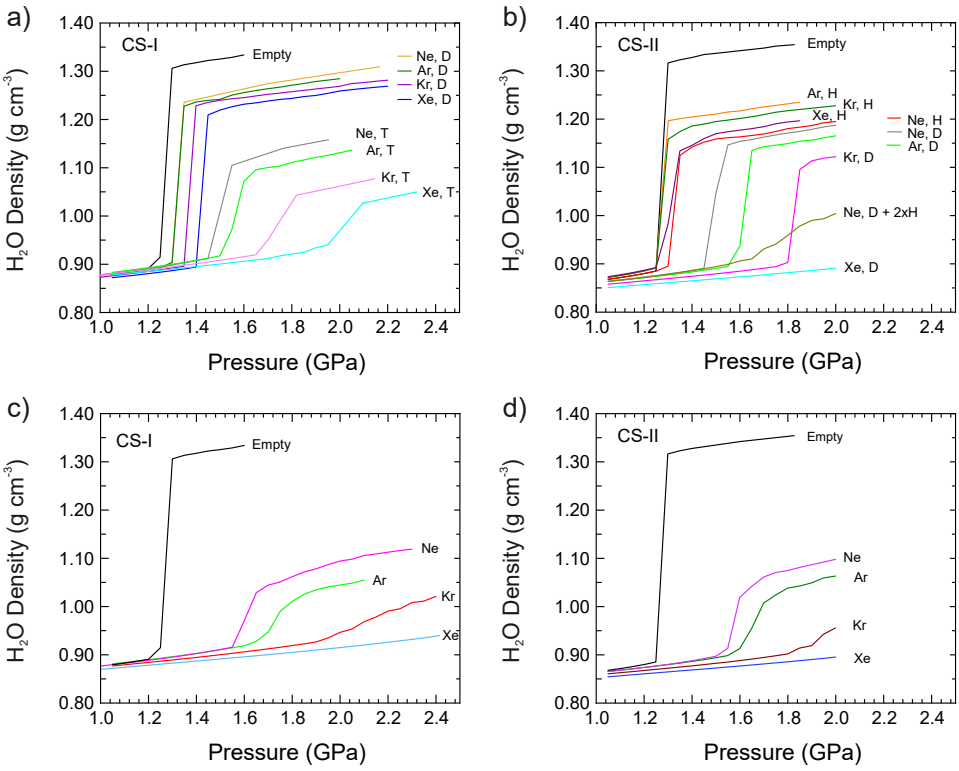

Figure 5.3.4: MD derived density-pressure relations for CS-I and CS-II Ng-CHs at 95 K considering different cage fillings. (a) Empty CS-I and Ne–Xe CHs with only T or only D cages filled. (b) Empty CS-II (ice XVI) and Ne–Xe CHs with only D or only H cages filled. CS-II Ne-CH with only H cages doubly occupied (red line) and D cages singly occupied and H cages doubly occupied (olive line). (c) CS-I and (d) CS-II Ng-CHs at 95 K. Both types of cages in each structure are completely filled, i.e., the compositions correspond to $Ng \cdot 5.75\,H_2O$ for CS-I and $Ng \cdot 5.67\,H_2O$ for CS-II. Adapted from Paper IV.

5.4 LT Compression of Low-Z CHs

H_2-CH and Ne-CH share the same clathrate structure as Ar-CH and THF-CH, but are distinguished because of the smaller-sized guests. The synthesis of low-Z CHs requires rather extreme pressure conditions (>0.2 GPa at 250 K), as discussed in Chapter 3. Compositions are also different, $H_2 \cdot \sim 4.2\,H_2O$ and $Ne \cdot \sim 4\,H_2O$, due to multiple occupancy in H cages. It was thus important to investigate how the pressure-behaviour of CHs with low-Z guests deviate from the systems previously discussed.

Fully deuterated H_2-CH and Ne-CH were studied by *in situ* ND upon LT compression. Figure 5.4.1 shows the evolution of the diffraction patterns for both CH up to 2.5–3 GPa around 95 K.

PIA of Ne-CH occurred at 1.9 GPa, following the established trend of Ng-CHs as discussed earlier. The pressure-induced collapse of Ne-CH was predicted by MD at ca. 1.6–1.8 GPa accounting for multiple occupancy of H cages (cf. Figure 5.3.4(b)). H_2-CH, on the other hand, assumed a highly disordered state near 1 GPa. In all attempts of compression between 95–200 K, it gradually transitioned to the filled-ice II structure (termed C_1 phase).

The CS-II $\rightarrow$ C_1 transition was reversible upon recovery to atmospheric pressure (at 95 K) and the composition remained constant. At slower compression rates, the CS-II H_2-CH was retained to 2.2(1) GPa. Although highly strained, the diffraction patterns above 1.5 GPa showed clear remnant features of the CS-II phase alongside growing reflections of the C_1 phase. H_2-CH never formed a fully amorphous state. Above 3 GPa a gradual decomposition into C_2 phase ($H_2 \cdot H_2O$, filled ice I_c) and ice VIII took place.

The extracted bulk moduli in the pressure range up to 1.5 GPa for H_2-CH and Ne-CH are 10.9(6) and 12(2) GPa, respectively, which follows the general trend.

CHs with low-Z guests can form distinct hydrate phases compared to Ar:H_2O, THF:H_2O, and other CHs with larger guest species. This is due to the unique ability of small species to penetrate the channel structures of ices II (C_1 structure) and I_c (C_2 structure), as well as another non-clathrate hydrate termed C_0.

The stability of CS-II and other phases is relevant to the formation of amorphous states. It is worth noting that CS-II Ne-CH is possibly at a limitrophe state on forming Ne-CH-HDA. In Chapter 6, we will explore how temperature can modify amorphous structures to allow the recovery of amorphous CHs. However, when Ne-CH-HDA was heated, it transformed into a FIS analogous to ice I_c, C_2 Ne hydrate.

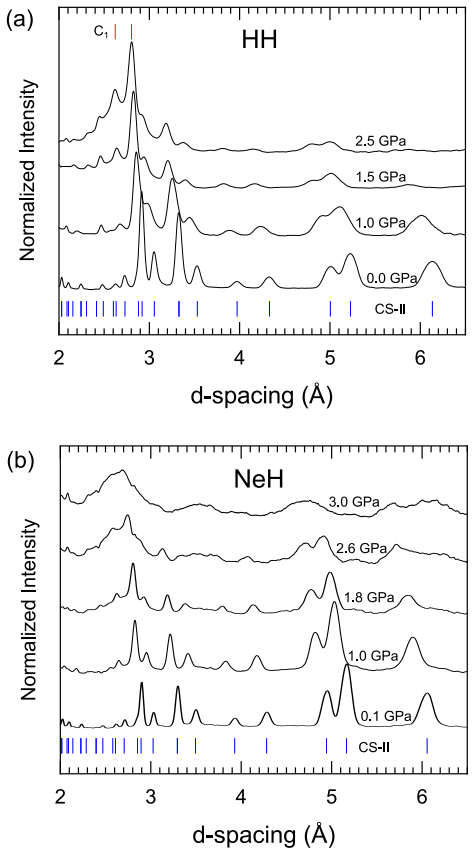

Figure 5.4.1: ND profiles of (a) H_2-CH and (b) Ne-CH upon compression up to 2.5–3.0 GPa. Tick marks show Bragg positions of allowed reflections for the CS-II phase at atmospheric pressure (blue ticks) and C_1 phase most intense reflections at 2.5 GPa (red ticks). Extract from Paper V.

5.5 Summary

Water-rich CHs (CS-II, 1:17 composition) showed a similar pressure-behaviour leading to complete amorphization at 1.1 GPa, 130 K. CS-II Ar-CH (1:6.5) amorphized at 1.4 GPa, 95 K. The discrepancy can be partly attributed to the lower temperature at which the Ar-CH experiment was performed, and partly to the stabilizing influence of the filled D cages. Xe-CH has a similar composition to Ar-CH, both types of cages filled to ca. 90%, but a different structure, CS-I. Xe-CH amorphized at much higher pressure, 4 GPa, representing also a unique case forming a semi-crystalline state before complete amorphization.

Simulations and experiments showed that the occupancy of cages (D cages in CS-II and both cages in CS-I) shifts PIA to successively higher pressures with increasing guest size. Deuteration showed no effect to PIA.

Similarly, the compressibility (expressed by the bulk modulus) of CHs increases with larger guests. Bulk moduli of both CS-I and CS-II, in most cases, are close to each other and were mainly determined by the elasticity of the hydrogen-bonded framework. Large guests such as Xe capable of influencing on the hydrogen-bond strength thus increased the bulk modulus of the CH. The presence of empty cages in water-rich CHs, on the other hand, decreases the bulk modulus.

It is clear that PIA in CHs follow a general trend, influenced by the size of the guest and occupancy of cages. Low-Z CHs are exceptional with stable FIS at high pressure and low temperature. All CH-HDA recrystallized on recovery attempts. Discussions on the local structure of CH amorphs and relation to their recoverability will follow in Chapter 6.

6

Distinct Structures of Amorphous CHs

Amorphous CHs might relate to a frozen solution of the guest, as an aqueous solution in which guest species are dissolved in an amorphous ice matrix [88]. However, the structure of the obtained CH-HDA has not been completely elucidated since (unlike water-ice) it reverts back to the original crystalline structure on pressure release.

There are several questions related to amorphous CHs: why is it not possible to recover CH-HDA? Are there distinct forms of amorphs as for water-ice? And if so, how are amorphous CH states related to amorphous ices?

Whereas the previous chapter dealt with the PIA phenomenon creating CH-HDA, this chapter summarizes *in situ* investigations using ND, thermal analysis and MD simulations intended to elucidate the structures of CH amorphs and answer these questions. In Paper VI three distinct amorphous forms arising from Ar-CH-HDA are further explored and structurally unveiled. Paper VII collects THF-CH studies to then elucidate the distinct amorphous states in the case of a large (and hydrogen-bonding) guest. The results are put into perspective with respect to Ar-CH armorphs and water-ice. Finally in Paper VIII the glass transitions amorphous CHs undergo when annealed are analyzed and discussed.

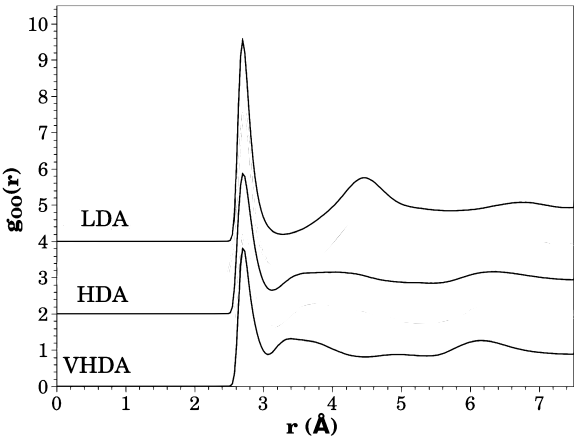

Figure 6.1.1: Oxygen–oxygen PDFs for three samples of amorphous ice: LDA, HDA, and VHDA. Adapted from Loerting et al. [89].

6.1 Background

The structure of HDA-ice relates to liquid water. HDA is also distinct from other amorphous structures of water-ice, LDA [35] and VHDA [34]. The existence of distinct amorphous phases (referred to as polyamorphism in Chapter 1) suggests the possibility of distinct high- and low-density liquid states of water, which helps explain several anomalies in the liquid water behaviour.

Mishima et al. [33] demonstrated first the capability of water-ice in forming structurally different amorphs. As introduced in Section 1.4, Ice I_h transforms into HDA ice upon compression below 140 K [33], and into VHDA ice after HDA is heated isobarically above 1 GPa [34]. Upon decompression, HDA can be transformed to LDA if heated at atmospheric pressure to 150 K [35]. The main distinction between water-ice polyamorphs is between the first and second coordination shells surrounding water molecules, as Loerting et al. [89] showed in the experimental PDFs, Figure 6.1.1. Coordination numbers are obtained if PDFs are integrated over space. Water molecules in LDA are 4-coordinated and the interstices between first and second shells are empty. HDA and VHDA have an increased water coordination, 5 and 6, respectively. The increase in coordination reflects in the respective increase in density.

In investigations subsequent to the findings of Handa et al. [84] (who first confirmed PIA of CHs), it was expected that the phase behaviour of amorphous CHs should resemble that observed in water-ice. Tulk et al. [85] were the first to structurally elucidate CH-HDA (with CH_4 guest) confirming that a completely disordered water

matrix formed (whereas guests showed some degree of long-range ordering).

Suzuki [88], thus, investigated CH-HDA with respect to the possibility of also identifying polyamorphism in amorphous CHs. By heat-cycling THF-CH-HDA (from 77 K) to 150 K at 1.5 GPa, the author showed that the amorphous state is stabilized and becomes recoverable. The recovered amorph had crystalline domains and easily recrystallized as CH. More recently, Bauer et al. [86] revisited the procedure showing that annealing at higher pressure and temperature, 1.8 GPa, 180 K, produced a crystalline-free amorphous form completely recoverable as amorphous. Further, Tulk et al. [85] showed that CH_4-CH-HDA (derived from CS-I CH_4-CH) had an increased metastability region (up to 220 K between 1.5 and 4 GPa) when compared to pure ice.

Tulk et al. [85] with *in situ* ND and English and Tse [90] with MD reported the structures of amorphous CH_4-CH before and after annealing. Amorphous CH_4-CH appeared heterogeneous with two length scales evidenced by a split first diffraction peak in the neutron structure factors $\mathrm{S(Q)}$, which correlates with intermediate range (3–6 Å) structural organization. The different length scales were assigned to distinct water-water and guest-water correlations.

It has been established that inclusion compounds of water can form solid solutions. Pressure-amorphized CHs (referred to as CH-HDA) are completely amorphous state related to a guest:water solution obtained from PIA. This state can be transformed into CH-VHDA, a more relaxed and densified state. Only CH-VHDA is recoverable. This finding has only been established for a limited number of case studies, and its applicability to a broader context is yet to be determined. Further investigation is also needed to characterize and distinguish between the different amorphous states of CHs.

6.2 Three Distinct Amorphous Forms of Ar-CH

Pressure-amorphized Ar-CH, Ar-CH-HDA, was investigated with *in situ* total neutron scattering. Experiments were run at the SNAP beamline. Isotope substitution was also explored, so ^{36}Ar-CH was undertaken in identical experiments.

The Ar:H_2O system is unique in several aspects. As discussed in Chapter 4, Ar is a good proxy for other guests in CHs. Since the composition of the CS-II crystalline precursor is well characterized, the composition of the amorphous Ar-CH is also known. Furthermore, the isotope substitution used in Paper I can be also exploited in the structural elucidation of Ar-CH amorphs.

Figure 6.2.1(a) shows experimental and MD simulated neutron $\mathrm{S(Q)}$s of ^{36}Ar-CH-HDA. By following the protocol by Bauer et al. [86], Ar-CH-HDA was

annealed and formed the densified form, Ar-CH-VHDA. The latter was recoverable and transformed into a third state termed recovered amorphous (RA). Figures 6.2.1(b) and (c) show the neutron $\mathrm{S(Q)}$s of Ar-CH-VHDA and -RA, respectively.

The neutron structure factors, together with MD simulations, allowed the elucidation of the amorphous structures. As it is clear in Figure 6.2.1, the structures of the three amorphs were found to be distinctly different.

Ar hydration structures in the three amorphs can be visualized in real space when plotting the Ar–O running coordination numbers, $\mathrm{n_{ArO}}(r)$, shown in Figure 6.2.2. $\mathrm{n_{ArO}}(r)$ plots show the distinct Ar coordinations in Ar-CH-HDA, -VHDA, and -RA. It is noteworthy that when Ar atoms are distinguished by the original cage they were located in the CS-II crystal, CH-HDA stands out with distinct Ar environments. Intermediate range order is maintained in that the originally different Ar atoms of the crystalline precursor attain differently dense hydration structures. When Ar-CH-HDA is annealed (to Ar-CH-VHDA), the hydration structure of Ar guests becomes more evenly distributed. This is likely because the increase in temperature allows the water molecules to move and reorient more freely. A section of the modelled crystalline and amorphous structures of Ar-CH is presented in Figure 6.2.3 where these distinct coordinations are highlighted.

The local water structures of Ar-CH-HDA and -VHDA show some analogy to those of the corresponding amorphous ices, featuring H_2O molecules with higher coordination with neighboring molecules. The coordination increase is observed in $\mathrm{g_{OO}}(r)$ plots as an interstitial peak between the first and second coordination shells, as in the case of water-ice amorphs. At 2 GPa, Ar-CH-HDA constitutes 4- and 5-coordinated molecules, whereas the hydrogen-bond network of Ar-CH-VHDA contains in addition 6-coordinated H_2O molecules. This is illustrated in Figure 6.2.4. The water coordination in Ar-CH amorphs is considerably less dense than water-ice amorphs. Ar-CH-RA, however, possesses a strictly 4-coordinated H_2O network, unlike the recovered forms of water-ice HDA and VHDA, which retain the increased water coordinations.

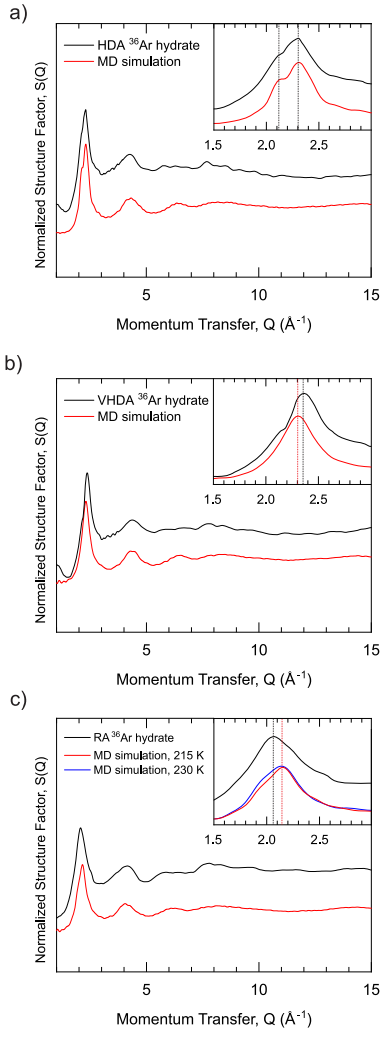

Figure 6.2.1: Experimental and MD simulated neutron structure factors, $\mathrm{S(Q)}$, for amorphous Ar-CH samples with ^{36}Ar and ^{2}H isotope substitution at 95 K. (a) Ar-CH-HDA at 2 GPa; (b) Ar-CH-VHDA at 2 GPa; and (c) Ar-CH-RA at atmospheric pressure. In (c) MD simulations are shown from systems after temperature cycling to 215 K (red line) and 230 K (blue line). Insets emphasize the region of the first diffraction peak, 1.5–3.0 Å^{-1}. Extract from Paper VI.

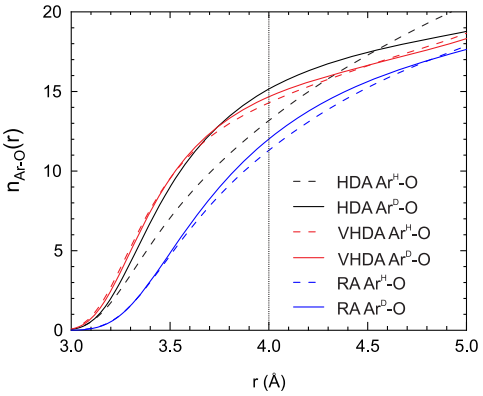

Figure 6.2.2: Running coordination numbers of Ar–O pairs for Ar-CH-HDA at 2 GPa, 95 K; Ar-CH-VHDA at 2 GPa, 95 K; and Ar-CH-RA at atmospheric pressure, 95 K. Ar coordinations are discriminated as Ar^H and Ar^D, corresponding to their original location in the crystalline CS-II. Extract from Paper VI.

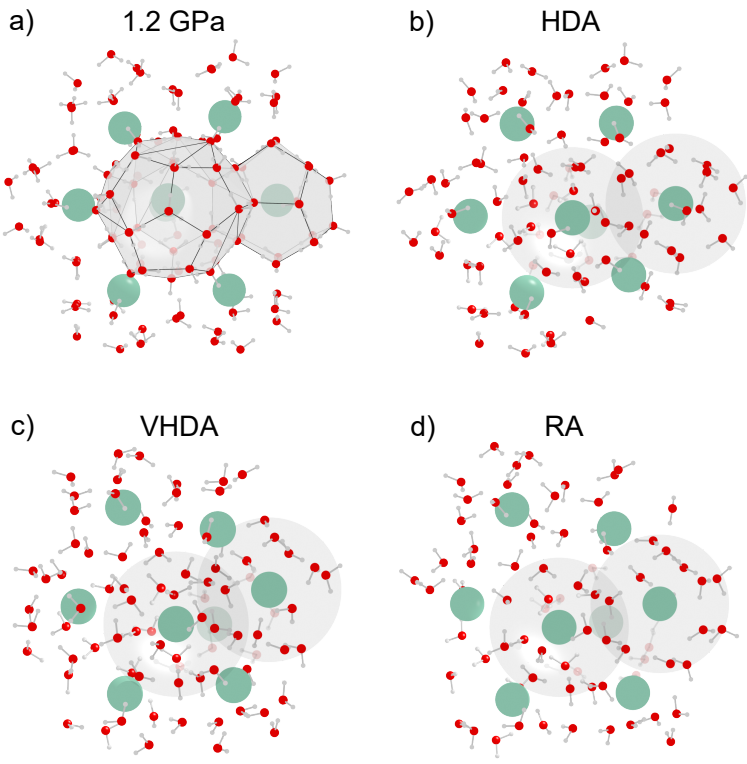

Figure 6.2.3: MD snapshots for Ar-CH at 95 K. (a) Crystalline CS-II at 1.2 GPa; (b) Ar-CH-HDA at 2.0 GPa; (c) Ar-CH-VHDA at 2.0 GPa after temperature cycling to 215 K; and (d) Ar-CH-RA at atmospheric pressure. Atoms are shown as spheres (red: oxygen, light-gray: hydrogen, green: argon). Gray areas emphasize Ar–water coordinations, H and D cages in crystalline CS-II and spheres at a 4 Å radius for the amorphous forms. Extract from Paper VI.

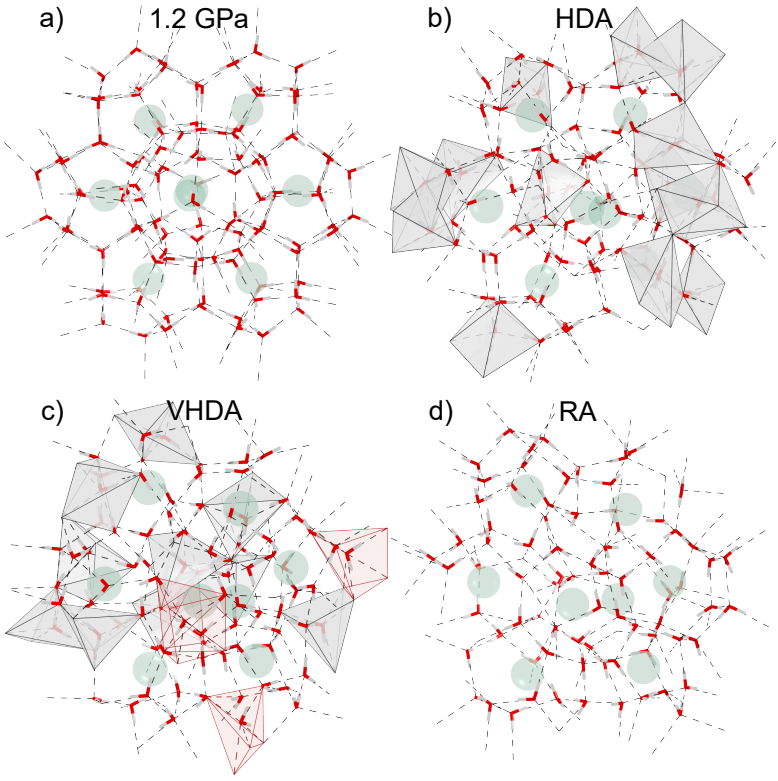

Figure 6.2.4: MD snapshots for Ar-CH at 95 K emphasizing the local water structure. (a) Crystalline CS-II at 1.2 GPa; (b) Ar-CH-HDA at 2.0 GPa; (c) Ar-CH-VHDA at 2.0 GPa after temperature cycling to 215 K; and (d) Ar-CH-RA at atmospheric pressure. Water molecules are depicted as "sticks" (red and white) and Ar atoms as faded-green spheres. Dashed lines show O–O distances up to 3.1 Å. 5- and 6-coordinated water molecules are highlighted as gray and red polyhedra, respectively. The latter are only present in CH-VHDA. Extract from Paper VI.

6.3 Distinct Amorphous Forms of THF-CH

Paper VII combines several ND experiments alongside MD simulations on amorphous THF-CH and a liquid solution of THF in water with the same concentration. The study focuses on the structural elucidation of THF-CH amorphs and compares its amorphous forms with Ar-CH and amorphous ices. The paper investigates the effect of the composition (cage occupancy) and guest species on the local water structures in the different forms of CHs. The results show that THF-CH-HDA is heterogeneous in nature, similar to Ar-CH-HDA, but for different reasons. THF-CH-HDA reverts to the crystalline CS-II structure upon decompression, while THF-CH-VHDA can be recovered (as THF-CH-RA) and both can be considered homogeneous solid solutions, the former denser and the latter less dense and like the liquid THF solution in water. The paper also highlights the influence of hydrogen bonding on guest hydration structures.

The compilation of experiments and MD simulations allowed full structural analysis of THF-CH amorphs. THF-CH-HDA appears heterogeneous with a split feature in the neutron $\mathrm{S(Q)}$. This is also the case in Ar-CH-HDA. The origin of the split feature in the latter comes from the distinct environments of Ar guests originally in D or H cages of the crystalline CH. Since THF-CH hosts guest only in H cages, the origin of the two length scales must be different.

Because the neutron $\mathrm{S(Q)}$ is dominated by oxygen and deuterium scattering, the two length scales indicate a denser and a less dense local water structure. This was first pointed out in Paper III, but the complete structural elucidation of THF-CH amorphs is reported only in Paper VIII.

MD simulations were then used to produce structures that help explain the neutron $\mathrm{S(Q)}$s. Figure 6.3.1 presents MD snapshots showing the THF hydration structure. THF molecules maintain a quasiregular array, reminiscent of the crystalline state, and their hydration structure (out to 5 Å) constitutes ca. 23 H_2O. The local water structure in THF-CH-HDA is reminiscent of pure HDA-ice, featuring 5-coordinated H_2O. In THF-CH-VHDA, this hydration structure is maintained but the local water structure is densified to resemble pure VHDA-ice with 6-coordinated H_2O. The hydration structure of THF in RA constitutes ca. 18 H_2O and the water structure corresponds to a strictly 4-coordinated network, as in the liquid solution.

Comparing the amorphous forms of THF-CH and Ar-CH, along with amorphous ices, enables general conclusions. In the Ar-CH system, both types of cages (small, D, and large, H cages) are occupied. Ar-Ar distances are much shorter (5.5–6.5 Å) than THF-THF, and Ar is a small guest species. With both types of cages filled, water is confined to a "thin-walled" porous space where the hydrogen-bond network accommodates simultaneously the guest's hydration structure. In contrast, the empty D

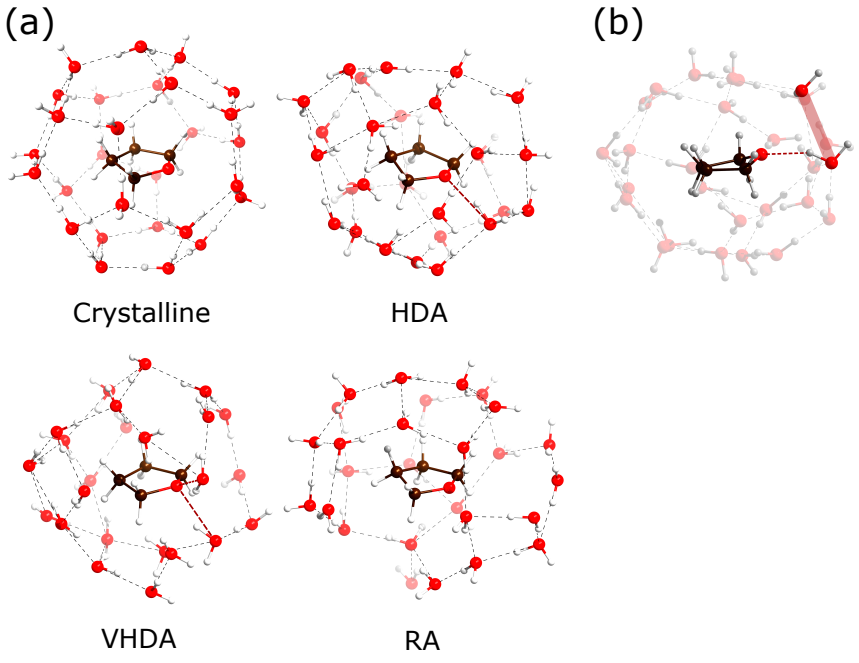

Figure 6.3.1: (a) MD snapshots showing the THF hydration structure for THF-CH systems at 130 K and 1 atm for crystalline and THF-CH-RA, and 2 GPa for THF-CH-HDA and THF-CH-VHDA. Atoms are shown as spheres (red: oxygen, white: hydrogen; brown: carbon). Dashed lines represent hydrogen bonds between water molecules (gray) and ether-O and water (red). (b) Same snapshot as THF-CH-HDA in (a) rotated for clarity. Extract from Paper VII.

cages in THF-CH give rise to "thick-walled" porous space with a more "independent" water structure – with a (small) fraction of water molecules not involved in guest coordination.

Figure 6.3.2 summarizes the local environments of Ar-CH and THF-CH as compared to water-ice. The local water structure of water-rich (1:17) amorphous CHs resembles most that of the corresponding amorphous water ices when compared to guest-rich CHs, e.g., Ar-CH (1:$\sim$6). Neutron structure factors evidence different length scales that come from distinct cage environments, in the case of Ar-CH, or the effect of guest-host interactions in THF-CH.

The influence of hydrogen bonding guests in the structures of amorphous CHs could

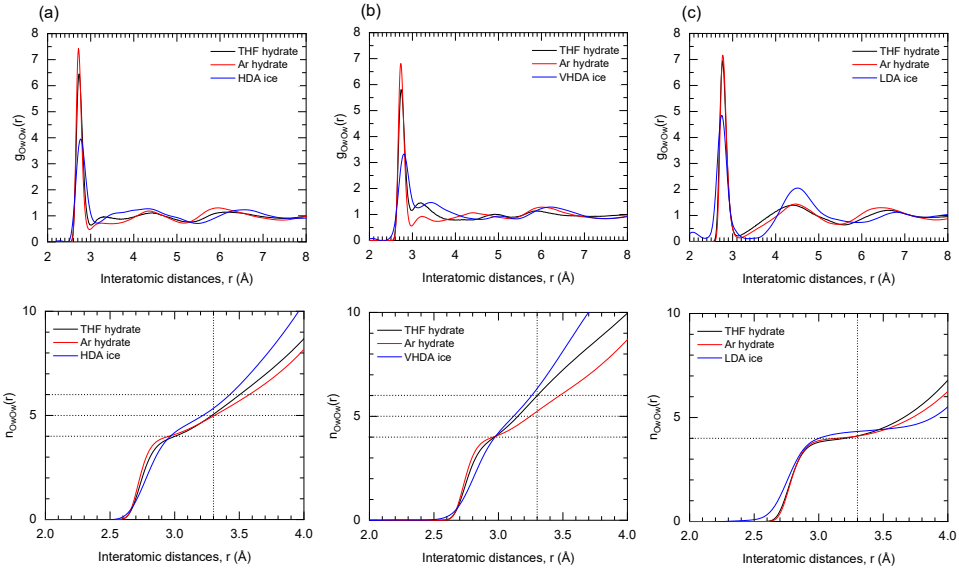

Figure 6.3.2: Partial PDFs and running coordination numbers from MD simulations for oxygen–oxygen pairs of (a) THF-CH-HDA, (b) THF-CH-VHDA and (c) THF-CH-RA compared to the analogous amorphous Ar-CH (Paper VI) and to amorphous ice data (at atmospheric pressure, Mariedahl et al. [91]). Extract from Paper VII.

not be separated from the water-rich composition of THF-CH. Investigation on little-interacting guests which also form water-rich CHs, such as SF_6 and cyclopentane, could clarify such influence.

6.4 Glass Transitions in Pressure-Amorphized CHs

Paper VIII explores the thermal and dielectric properties of amorphous CHs to investigate glass transitions.

It is usually possible to study the change from a low-viscosity liquid to a supercooled (metastable) high-viscosity liquid, and the subsequent transformation into a glass (an amorphous state) which is characterized by a glass transition temperature T_g. In addition to the increase in viscosity, a glass transition can be characterized by a sigmoid-shaped decrease in heat capacity. This effect originates from the arrest of structural fluctuations. Such fluctuations involve translational motion and reorientational motion. Normally both occur simultaneously at T_g.

Water, however, crystallizes above T_g. The region of water's phase diagram where crystallization is unavoidable ('no man's land') is a convergence point where many anomalies in supercooled and amorphous water can't be investigated. Being able to investigate structure and dynamics of liquid or amorphous water in 'no man's land' is essential for a comprehensive understanding of water and assessing existing theories about its anomalies.

Amorphous CHs have an increased metastability region and offer a gateway to probing such temperature-pressure regions unachievable in a pure-water system. The existing similarities between PIA and densification processes of amorphous CHs and water-ice indicate that the glass transitions in both systems may be related to the same transformations in water structure.

In Paper VIII, it is evidenced that water, in a water-rich homogeneous solution, is a rare example where the processes of translational and reorientational mobility freezing are significantly shifted in temperature.

Pressure-amorphized CHs with THF, cyclobutanone and 1,3-dioxolane as guests were investigated on heating in the 0.2–0.7 GPa range. All CH amorphs showed two glass transitions with indistinguishable characteristics as that of water-ice amorphs. The first glass transition near 130 K shows a weak and gradual heat capacity increase and occurs at a temperature similar to that of HDA-ice. The second glass transition is associated with a large heat capacity increase. It implies a transformation to an ultraviscous liquid on heating. Deuteration of water shifts the transitions to higher temperatures. Both deuteration of the guest and exchange of the guest (between THF, cyclobutanone and 1,3-dioxolane) don't seem to affect the glass transitions.

The glass transitions observed in amorphous CHs are observed at identical temperatures as compared to that observed for water-ice. The related heat capacity increase is the same, and it occurs over an unusually wide (identical) temperature range. These results establish that the glass transitions in amorphous CHs are due to kinetic unfreezing of water molecules and are not associated with the guest mobility.

7

Summary and Prospects

Clathrate hydrates (CHs) are crystalline inclusion compounds, in which water molecules form hydrogen-bonded networks that encapsulate species within it. CHs are important storage materials and may form naturally or synthetically with various guests e.g., tetrahydrofuran (THF), noble gases and H_2. CH structures vary with formation conditions and also with guest nature. Typically CHs form with the cubic structures I (CS-I) and II (CS-II).

A deeper understanding of the guest disorder in CS-II Ar-CH was sought using isotope substitution ($Ar/^{36}Ar$) neutron diffraction (ND). Results allowed the guest distribution in the clathrate structure to be resolved and provided a better model for the structure of CS-II Ar-CH. The crystalline material was investigated in the temperature range 20–90 K and compared to similar-sized guests in the same clathrate structure. Guest-host interactions in CHs appear very similar and the nature of guests don't affect the thermal behaviour of CHs.

The behaviour of CHs when subjected to high pressure was explored. Experiments (ND and thermal analysis) and molecular dynamics simulations were conducted to observe how the structure of CHs changed under increasing pressure. The crystalline form of the clathrates can be transformed into an amorphous form at high enough pressure. This form cannot be recovered and recrystallizes upon pressure release. This transformation on compression, known as pressure-induced amorphization (PIA), results in the loss of the regular, repeating structure of the clathrate. This thesis introduces a generalization of the PIA of CHs.

An investigation into the structure of amorphous CHs used methods to achieve a recoverable amorphous CH form and this thesis studies the various distinct amorphous structures obtained. The study looked at both Ar-CH and THF-CH systems with CS-II and found that there are three distinct polyamorphs derived from crystalline CH:

- CHs undergo PIA when compressed to 1–5 GPa in the temperature range 77–140 K to form high-density amorphous (CH-HDA). CH-HDA is heterogeneous in nature, evidenced in neutron structure factors $\mathrm{S(Q)}$. Guest species in CH-HDA maintain a quasi-regular arrangement, similar to the crystalline state. The local water structure in CH-HDA resembles pure HDA-ice with increased coordination. The hydration structure of guests differs with composition, water-rich amorphs enabling a higher water coordination.

- Very-high-density amorphous (CH-VHDA) is derived from CH-HDA by heat-cycling at high pressure to 180 K. CH-VHDA has a denser local water structure than CH-HDA, resembling pure VHDA-ice with 6-coordinated H_2O. The water coordination in Ar-CH amorphs is considerably less dense than amorphous ices. Distinctions in the hydration structure surrounding guest species are evened out.

- Recovered amorphous (CH-RA) is obtained from CH-VHDA after pressure release. Water is strictly 4-coordinated which is unlike the recovered forms of water-ice HDA and VHDA. This state resembles liquid solutions of guest in water. Both CH-VHDA and CH-RA are homogeneous representing denser and less dense solid solutions of guest and water, respectively.

It is likely that CH-HDA reverts to crystalline CH on pressure release because it retains the distinction of cage environments surrounding guest species. The transformation between CH-HDA to CH-VHDA eliminates this distinction. These results are specific to CS-II CHs. The recoverability of amorphous CS-I CHs requires further investigation.

The bulk moduli of crystalline CHs are determined by the hydrogen-bonded framework and are influenced by guest species.

A combination of ND and thermal analysis was used with focus on the glass transition behaviour of CHs. Evidence was shown suggesting that the water mobility in these materials (particularly water-rich CHs) undergoes two distinct glass transitions. The glass transitions in amorphous CHs are not associated with the guest mobility.

CHs with low-Z guests were shown to undergo crystal-crystal transformations even at temperatures below 200 K and were not comparable to other CHs. Although Ne-CH-HDA was produced, Ne-CH-VHDA could not be produced. H_2-CH never

transformed into a fully amorphous state.

Further investigation on systems such as amorphous CS-I CHs or CS-II with guests e.g., cyclopentane and SF_6 may help answer a few remaining questions. Amorphous CHs are poorly explored materials that here offer a linking pathway between amorphous states of ice and the complex nature of water.

Acknowledgements

I would like to express my sincere gratitude to my supervisor, Ulrich Häussermann, for his invaluable guidance, encouragement and support throughout my Ph.D. studies. I am also grateful to Ove Andersson, my co-supervisor, for his valuable insights and inspiring projects that have broadened my horizons.

I extend my appreciation to the opponent, members of the defense committee and chair: Doc. John Loveday, Doc. Anita Zeidler, Prof. Lars Pettersson, Doc. Martin Månsson, Doc. Andrew Ken Inge and Doc. Anneli Kruve.

I am grateful to Jekabs Grins (whom I've quoted in the introduction of this thesis) for his insightful advice, wisdom and generosity, and to Arnold Maliniak for his everlasting energy, positivity and support. I am indebted to all my collaborators and colleagues who have contributed to my research in various ways. In particular, I would like to thank Chris Tulk, Bianca Haberl, Luke Daemen, Jamie Molaison and the SNAP and Sample Environment teams at ORNL, Craig Bull, Nick Funnell, Pedro Moraes, Alexandre Leitão, Amber Mace, Mikhail Ivanov, Alexander Lyubartsev, Katrin Amann-Winkel and Thomas Loerting for their expertise, patience and support.

My colleagues at MMK and SwedNess and my friends, who have made my Ph.D. journey more enjoyable and memorable. My family who motivated me and endured the distance. Their unwavering love and encouragement have been my main source of strength and inspiration.

Bibliography

[1] Sloan Jr., E.D. and Koh, C.A. (2008) Clathrate hydrates of natural gases. Boca Raton, FL: CRC Press.

[2] Ripmeester, J.A. and Alavi, S. (2022) Clathrate hydrates. Weinheim, Germany: Wiley-VCH.

[3] Davy, H. (1811) "Viii. on a combination of oxymuriatic gas and Oxygene Gas" Philosophical Transactions of the Royal Society of London, 101, pp. 155–162.

[4] Ripmeester, J.A. et al. (1994) "Molecular perspectives on structure and dynamics in clathrate hydrates," Annals of the New York Academy of Sciences, 715(1 Natural Gas H), pp. 161–176.

[5] Matsumoto, R. (2001) "Methane hydrates," Encyclopedia of Ocean Sciences, pp. 1745–1757.

[6] Osegovic, J.P. and Max, M.D. (2005) "Compound clathrate hydrate on Titan's surface," Journal of Geophysical Research: Planets, 110(E8).

[7] Ghosh, J. et al. (2019) "Clathrate hydrates in interstellar environment," Proceedings of the National Academy of Sciences, 116(5), pp. 1526–1531.

[8] Mao, W.L. et al. (2002) "Hydrogen clusters in clathrate hydrate," Science, 297(5590), pp. 2247–2249.

[9] Jamaluddin, A.K.M., Kalogerakis, N. and Bishnoi, P.R. (1991) "Hydrate plugging problems in undersea natural gas pipelines under shutdown conditions," Journal of Petroleum Science and Engineering, 5(4), pp. 323–335.

[10] Milkov, A.V. (2004) "Global estimates of Hydrate-Bound Gas in marine sediments: How much is really out there?," Earth-Science Reviews, 66(3-4), pp. 183–197.

[11] Harvey, L.D. and Huang, Z. (1995) "Evaluation of the potential impact of methane clathrate destabilization on future global warming," Journal of Geophysical Research, 100(D2), p. 2905.

[12] Ogienko, A.G. et al. (2022) "Clathrate hydrates of organic solvents as auxiliary intermediates in pharmaceutical research and development: Improving dissolution behaviour of a new anti-tuberculosis drug, Perchlozon," Pharmaceutics, 14(3), p. 495.

[13] Babu, P. et al. (2018) "A review of clathrate hydrate based desalination to Strengthen Energy–Water Nexus," ACS Sustainable Chemistry Engineering, 6(7), pp. 8093–8107.

[14] Peng, X. et al. (2010) "Separation of ionic liquids from dilute aqueous solutions using the method based on CO_2 Hydrates," Journal of Natural Gas Chemistry, 19(1), pp. 81–85.

[15] Merriam-Webster.com Dictionary, s.v. "clathrate," accessed January 18, 2023, https://www.merriam-webster.com/dictionary/clathrate.

[16] Loveday, J.S. and Nelmes, R.J. (2008) "High-pressure gas hydrates," Phys. Chem. Chem. Phys., 10(7), pp. 937–950.

[17] Shin, K. et al. (2013) "Methanol incorporation in clathrate hydrates and the implications for oil and gas pipeline flow assurance and Icy Planetary Bodies," Proceedings of the National Academy of Sciences, 110(21), pp. 8437–8442.

[18] Fässler Thomas (2013) Zintl phases: Principles and recent developments. Berlin: Springer.

[19] Stackelberg, M.v. and Müller, H.R. (1951) "On the structure of gas hydrates," The Journal of Chemical Physics, 19(10), pp. 1319–1320.

[20] Bernal, J.D. and Fowler, R.H. (1933) "A theory of water and Ionic solution, with particular reference to hydrogen and hydroxyl ions," The Journal of Chemical Physics, 1(8), pp. 515–548.

[21] Davidson, D.W. (1971) "The motion of guest molecules in clathrate hydrates," Canadian Journal of Chemistry, 49(8), pp. 1224–1242.

[22] Andersson, O. and Johari, G.P. (2008) "Collapse of an ice clathrate under pressure observed via thermal conductivity measurements," Physical Review B, 78(17).

[23] Tanaka, H. and Amano, Y. (2002) "Pressure-induced amorphization of clathrate hydrates," Molecular Physics, 100(14), pp. 2183–2188.

[24] Bondi, A. (1964) "Van der Waals volumes and radii," The Journal of Physical Chemistry, 68(3), pp. 441–451.

[25] Holder, G.D. and Manganiello, D.J. (1982) "Hydrate dissociation pressure minima in Multicomponent Systems," Chemical Engineering Science, 37(1), pp. 9–16.

[26] Patchkovskii, S. and Tse, J.S. (2003) "Thermodynamic stability of hydrogen clathrates," Proceedings of the National Academy of Sciences, 100(25), pp. 14645–14650.

[27] Manakov, A.Y. et al. (2004) "Structural investigations of argon hydrates at pressures up to 10 kbar," Journal of Inclusion Phenomena, 48(1/2), pp. 11–18.

[28] Hirai, H. et al. (2002) "Structural changes of argon hydrate under high pressure," The Journal of Physical Chemistry B, 106(43), pp. 11089–11092.

[29] Manakov, A.Y. et al. (2011) "High-pressure gas hydrates of argon: Compositions and equations of State," The Journal of Physical Chemistry B, 115(31), pp. 9564–9569.

[30] Schaack, S. et al. (2019) "Observation of methane filled hexagonal ice stable up to 150 GPa," Proceedings of the National Academy of Sciences, 116(33), pp. 16204–16209.

[31] Hirai, H. et al. (2012) "Structural changes of filled ice I_c hydrogen hydrate under low temperatures and high pressures from 5 to 50 GPa," The Journal of Chemical Physics, 137(7), p. 074505.

[32] Ranieri, U. (2018) "Guest dynamics in methane hydrates and hydrogen hydrates under high pressure", Ph.D. thesis, EPFL, Lausanne, Switzerland.

[33] Mishima, O., Calvert, L.D. and Whalley, E. (1984) "'melting ice' I at 77 K and 10 kbar: A new method of making amorphous solids," Nature, 310(5976), pp. 393–395.

[34] Mishima, O. (1994) "Reversible first-order transition between two H_2O amorphs at $\sim$0.2 GPa and $\sim$135 K," The Journal of Chemical Physics, 100(8), pp. 5910–5912.

[35] Winkel, K. et al. (2008) "Water polyamorphism: Reversibility and (dis)continuity,"

The Journal of Chemical Physics, 128(4), p. 044510.

[36] Poole, P.H. et al. (1997) "Polymorphic phase transitions in liquids and glasses," Science, 275(5298), pp. 322–323.

[37] McMillan, P.F. et al. (2007) "Polyamorphism and Liquid–Liquid Phase Transitions: Challenges for experiment and theory," Journal of Physics: Condensed Matter, 19(41), p. 415101.

[38] Hemley, R.J. et al. (1988) "Pressure-induced amorphization of crystalline silica," Nature, 334(6177), pp. 52–54.

[39] Loerting, T. et al. (2011) "How many amorphous ices are there?," Physical Chemistry Chemical Physics, 13(19), p. 8783.

[40] Kuhs, W.F., Hansen, T.C. and Falenty, A. (2018) "Filling ices with helium and the formation of helium clathrate hydrate," The Journal of Physical Chemistry Letters, 9(12), pp. 3194–3198.

[41] Sloan, E.D. (2003) "Fundamental principles and applications of natural gas hydrates," Nature, 426(6964), pp. 353–359.

[42] Sengupta, S. et al. (2015) "Exploring dynamics and cage–guest interactions in clathrate hydrates using solid-state NMR," The Journal of Physical Chemistry B, 119(50), pp. 15485–15492.

[43] Dyadin, Y.A. et al. (1999) "Clathrate hydrates of hydrogen and Neon," Mendeleev Communications, 9(5), pp. 209–210.

[44] Falenty, A., Hansen, T.C. and Kuhs, W.F. (2014) "Formation and properties of Ice XVI obtained by emptying a type sII clathrate hydrate," Nature, 516(7530), pp. 231–233.

[45] del Rosso, L., Celli, M. and Ulivi, L. (2016) "New porous water ice metastable at atmospheric pressure obtained by emptying a hydrogen-filled ice," Nature Communications, 7(1).

[46] Komatsu, K. et al. (2020) "Ice I_c without stacking disorder by evacuating hydrogen from hydrogen hydrate," Nature Communications, 11(1).

[47] Byrne, J. (2011) Neutrons, nuclei, and matter: An exploration of the physics of slow neutrons. Mineola, NY: Dover Publications.

[48] Chadwick, J. (1932) "Possible existence of a neutron," Nature, 129(3252), pp. 312–312.

[49] De Angelis, A. (2013) "Spontaneous ionization to subatomic physics: Victor Hess to Peter Higgs," Nuclear Physics B - Proceedings Supplements, 243-244, pp. 3–11.

[50] Guthrie, M. (2015) "Future directions in high-pressure neutron diffraction," Journal of Physics: Condensed Matter, 27(15), p. 153201.

[51] Willis, B.T.M. and Carlile, C.J. (2013) Experimental neutron scattering. Oxford: Oxford University Press.

[52] Sears, V.F. (1992) "Neutron scattering lengths and cross sections," Neutron News, 3(3), pp. 26–37.

[53] Rietveld, H.M. (1967) "Line profiles of neutron powder-diffraction peaks for structure refinement," Acta Crystallographica, 22(1), pp. 151–152.

[54] Parker, S.F. et al. (1997) "Inelastic neutron scattering, infrared, and Raman spectroscopic studies of Mg_2FeH_6 and Mg_2FeD_6," Inorganic Chemistry, 36(23), pp. 5218–5221.

[55]Fujita, F.E. (1985) "A theory of medium range order in supercooled liquid and amorphous solid metals," Rapidly Quenched Metals, pp. 585–588.

[56] Andersson, O. and Inaba, A. (2006) "Dielectric properties of high-density amorphous ice under pressure," Physical Review B, 74(18).

[57] Andersson, O. and Inaba, A. (2005) "Thermal conductivity of crystalline and amorphous ices and its implications on amorphization and glassy water," Physical Chemistry Chemical Physics, 7(7), p. 1441.

[58] Andersson, O. and Häussermann, U. (2018) "A second glass transition in pressure collapsed type II clathrate hydrates," The Journal of Physical Chemistry B, 122(15), pp. 4376–4384.

[59] Håkansson, B., Andersson, P. and Bäckström, G. (1988) "Improved hot-wire procedure for thermophysical measurements under pressure," Review of Scientific Instruments, 59(10), pp. 2269–2275.

[60] Podlesnyak, A. et al. (2018) "Clamp cell with in situ pressure monitoring for

low-temperature neutron scattering measurements," High Pressure Research, 38(4), pp. 482–492.

[61] Shi, Y. et al. (2019) "High-pressure neutron diffraction techniques based on Paris-Edingburgh Press," Acta Physica Sinica, 68(11), p. 116101.

[62] Bull, C.L. et al. (2016) "Pearl: The high pressure neutron powder diffractometer at Isis," High Pressure Research, 36(4), pp. 493–511.

[63] Abraham, M.J. et al. (2015) "Gromacs: High performance molecular simulations through multi-level parallelism from laptops to supercomputers," SoftwareX, 1-2, pp. 19–25.

[64] Plimpton, S. (1995) "Fast parallel algorithms for short-range molecular dynamics," Journal of Computational Physics, 117(1), pp. 1–19.

[65] Thompson, A.P. et al. (2022) "LAMMPS - a flexible simulation tool for particle-based materials modeling at the Atomic, Meso, and continuum scales," Computer Physics Communications, 271, p. 108171. See `http://lammps.sandia.gov` for information about the LAMMPS software.

[66] Matsumoto, M., Yagasaki, T. and Tanaka, H. (2017) "Genice: Hydrogen-disordered Ice Generator," Journal of Computational Chemistry, 39(1), pp. 61–64.

[67] Li, L. et al. (2020) "Unraveling nucleation pathway in methane clathrate formation," Proceedings of the National Academy of Sciences, 117(40), pp. 24701–24708.

[68] Mohammadi, A.H. and Richon, D. (2011) "Ice–clathrate hydrate–gas phase equilibria for argon + water and carbon dioxide + water systems," Industrial amp; Engineering Chemistry Research, 50(19), pp. 11452–11454.

[69] Ohgaki, K. et al. (2000) "Phase behavior of Xenon Hydrate System," Fluid Phase Equilibria, 175(1-2), pp. 1–6.

[70] Dyadin, Y.A. et al. (1999) "Clathrate formation in water-noble gas (hydrogen) systems at high pressures," Journal of Structural Chemistry, 40(5), pp. 790–795.

[71] Stern, L.A. et al. (2004) "Scanning electron microscopy investigations of laboratory-grown gas clathrate hydrates formed from melting ice, and comparison to natural hydrates," American Mineralogist, 89(8-9), pp. 1162–1175.

[72] Kuhs, W.F. et al. (2000) "The formation of meso- and macroporous gas hydrates," Geophysical Research Letters, 27(18), pp. 2929–2932.

[73] Staykova, D.K. et al. (2003) "Formation of porous gas hydrates from ice powders: diffraction experiments and multistage model," The Journal of Physical Chemistry B, 107(37), pp. 10299–10311.

[74] Lokshin, K.A. and Zhao, Y. (2006) "Fast synthesis method and phase diagram of hydrogen clathrate hydrate," Applied Physics Letters, 88(13), p. 131909.

[75] Barrer, R.M. and Edge, A.V.J. (1967) "Gas hydrates containing argon, krypton and xenon: Kinetics and energetics of formation and equilibria" (1967) Proceedings of the Royal Society of London. Series A. Mathematical and Physical Sciences, 300(1460), pp. 1–24.

[76] Davidson, D.W. et al. (1984) "The ability of small molecules to form clathrate hydrates of structure II," Nature, 311(5982), pp. 142–143.

[77] Chazallon, B. and Kuhs, W.F. (2002) "in situstructural properties of N_2-, O_2-, and air-clathrates by neutron diffraction," The Journal of Chemical Physics, 117(1), pp. 308–320.

[78] Hansen, T.C., Falenty, A. and Kuhs, W.F. (2016) "Lattice constants and expansivities of gas hydrates from 10 K up to the Stability Limit," The Journal of Chemical Physics, 144(5), p. 054301.

[79] Yang, L. et al. (2010) "Guest disorder and high pressure behavior of argon hydrates," Chemical Physics Letters, 485(1-3), pp. 104–109.

[80] Itoh, H., Tse, J.S. and Kawamura, K. (2001) "The structure and dynamics of doubly occupied Ar Hydrate," The Journal of Chemical Physics, 115(20), pp. 9414–9420.

[81] Papadimitriou, N.I. et al. (2008) "Monte Carlo Study of sII and sH argon hydrates with multiple occupancy of cages," Molecular Simulation, 34(10-15), pp. 1311–1320.

[82] Chazallon, B. et al. (2002) "Anharmonicity and guest–host coupling in clathrate hydrates," Phys. Chem. Chem. Phys., 4(19), pp. 4809-4816.

[83] Ross, R.G. and Andersson, P. (1982) "Clathrate and other solid phases in the tetrahydrofuran–water system: Thermal conductivity and heat capacity under pressure,"

Canadian Journal of Chemistry, 60(7), pp. 881–892.

[84] Handa, Y.P. et al. (1991) "Pressure-induced phase transitions in clathrate hydrates," The Journal of Chemical Physics, 94(1), pp. 623–627.

[85] Tulk, C.A. et al. (2012) "Structure and stability of an amorphous water–methane mixture produced by cold compression of Methane Hydrate," Physical Review B, 86(5).

[86] Bauer, M. et al. (2011) "Pressure-amorphized cubic structure II clathrate hydrate: Crystallization in slow motion," Phys. Chem. Chem. Phys., 13(6), pp. 2167–2171.

[87] Strässle, T. et al. (2007) "Experimental evidence for a crossover between two distinct mechanisms of amorphization in ice I_h under pressure" Physical Review Letters, 99(17).

[88] Suzuki, Y. (2004) "Evidence of pressure-induced amorphization of tetrahydrofuran clathrate hydrate," Physical Review B, 70(17).

[89] Loerting, T. et al. (2011) "Cryoflotation: Densities of amorphous and crystalline ices," The Journal of Physical Chemistry B, 115(48), pp. 14167–14175.

[90] English, N.J. and Tse, J.S. (2012) "Pressure-induced amorphization of methane hydrate," Physical Review B, 86(10).

[91] Mariedahl, D. et al. (2018) "X-ray scattering and O–O pair-distribution functions of amorphous ices," The Journal of Physical Chemistry B, 122(30), pp. 7616–7624.